Shape-Controlled Synthesis of Colloidal Metal Nanocrystals: Thermodynamic versus Kinetic Products

Younan Xia,*[†,‡] Xiaohu Xia,[†,§] and Hsin-Chieh Peng[‡,§]

[†]The Wallace H. Coulter Department of Biomedical Engineering, Georgia Institute of Technology and Emory University, Atlanta, Georgia 30332, United States

[‡]School of Chemistry and Biochemistry, Georgia Institute of Technology, Atlanta, Georgia 30332, United States

ABSTRACT: This Perspective provides a contemporary understanding of the shape evolution of colloidal metal nanocrystals under thermodynamically and kinetically controlled conditions. It has been extremely challenging to investigate this subject in the setting of one-pot synthesis because both the type and number of seeds involved would be changed whenever the experimental conditions are altered, making it essentially impossible to draw conclusions when comparing the outcomes of two syntheses conducted under different conditions. Because of the uncertainty about seeds, most of the mechanistic insights reported in literature for one-pot syntheses of metal nanocrystals with different shapes are either incomplete or ambiguous, and some of them might be misleading or even wrong. Recently, with the use of well-defined seeds for such syntheses, it became possible to separate growth from nucleation and therefore investigate the explicit role(s) played by a specific thermodynamic or kinetic parameter in directing the evolution of colloidal metal nanocrystals into a specific shape. Starting from single-crystal seeds enclosed by a mix of {100}, {111}, and {110} facets, for example, one can obtain colloidal nanocrystals with diversified shapes by adjusting various thermodynamic or kinetic parameters. The mechanistic insights learnt from these studies can also be extended to account for the products of conventional one-pot syntheses that involve self-nucleation only. The knowledge can be further applied to many other types of seeds with twin defects or stacking faults, making it an exciting time to design and synthesize colloidal metal nanocrystals with the shapes sought for a variety of fundamental studies and technologically important applications.

1. INTRODUCTION

Metals are central to the development of modern science and technology. Many of them have already found extensive use in applications that range from catalysis[1] to electronics,[2] photonics,[3] information storage,[4] energy conversion/storage,[5] environmental protection,[6] and medicine.[7] Most of these applications require the use of metals in a finely divided state, preferably in the form of nanocrystals with at least one dimension in the range of 1−100 nm. Here we use the term "nanocrystal" rather than "nanoparticle" to emphasize the crystalline lattice taken by the atoms in such a miniscule structure. Although controlling the geometric shape taken by a metal nanocrystal may initially seem like a scientific curiosity, its implication goes far beyond aesthetic appeal. The shape not only controls its physicochemical properties but also determines its relevance and merit for the aforementioned applications.[8]

A fascinating example can be found in localized surface plasmon resonance (LSPR),[9] an optical phenomenon arising from the collective oscillation of free electrons in a nanocrystal made of a metal such as Au or Ag in response to the oscillating electric field of the incident light. Under resonance, the incident light can be effectively absorbed and converted to photons (scattering, at the same frequency but into all different directions) or phonons (absorption or photothermal conversion, to excite the vibrational modes of the crystal lattice). The number of resonance peaks, their wavelengths, and the ratio between scattering and absorption cross sections are all dependent on the geometric shape of the nanocrystal because this particular parameter determines how the polarization of free electrons occurs and how the charges are distributed on the surface. For Au nanospheres of 50 nm in diameter, the LSPR is dominated by a strong peak at ∼525 nm, giving their aqueous suspension (equivalent to the conventional Au colloids) a striking ruby red color as the green light is largely absorbed by the nanospheres and non-radioactively converted into heat.[10] For Au nanorods with dimensions of 10×50 nm^2 (width × length), on the other hand, there are two LSPR peaks. The peak associated with the oscillation of free electrons along the short axis is positioned at ∼540 nm while the mode along the long axis is peaked at ∼825 nm, giving their aqueous suspension a light brown color.[11] In addition to LSPR, the merit of Au or Ag nanocrystals for many other applications, including surface-enhanced Raman scattering and surface-enhanced fluorescence, can be greatly augmented by achieving a tight control over their geometric shapes.[12]

Heterogeneous catalysis is another interesting example. It has been established that many reactions on catalysts based on metal nanocrystals are highly sensitive, in terms of activity and/or selectivity, to the arrangement (or, more precisely, the coordination number) of atoms and thus the type of facet on the surface, which is determined by the geometric shape of the nanocrystals.[13] It has been reported that the hydrogenation of benzene catalyzed by 13 nm Pt cuboctahedrons covered by a mix of {111} and {100} facets generated both cyclohexane and cyclohexene, whereas only cyclohexene was produced on 13 nm Pt cubes encased by {100} facets.[14] For the oxygen reduction reaction (ORR), the catalytic activity of 6 nm Pd

cubes covered by {100} facets was found to be 1 order of magnitude higher than that of 6 nm Pd octahedrons covered by {111} facets.[15] In the case of Pt_3Ni alloy, the ORR activity of {111} facets on octahedral nanocrystals could be more than 50 times higher than the {100} facets on cubic counterparts.[16] Similar correlations between the catalytic activity/selectivity and the geometric shape (or more directly, the type of facet exposed on the surface) of nanocrystals have also been observed in many other systems.[17]

These and many other examples clearly illustrate the critical importance of shape control to the effective use of metal nanocrystals in a wide variety of applications. Thanks to the tremendous efforts from many research groups, the past decade has witnessed spectacular success in developing a myriad of methods for shape-controlled syntheses of colloidal metal nanocrystals.[18] Metal nanocrystals with many distinctive shapes can now be readily prepared, with notable examples including two-dimensional (2-D) nanocrystals such as thin plates or prisms with triangular, hexagonal, or circular projections; 1-D nanocrystals such as rods, bars, and wires with circular, square, rectangular or pentagonal cross sections; as well as 0-D nanocrystals such as spheres, spheroids, cubes, cuboctahedrons, octahedrons, tetrahedrons, rhombic dodecahedrons, bipyramids, decahedrons, and icosahedrons. In addition, nanocrystals with concave surfaces, facets of high Miller index (containing indices >1), or branched arms have also become increasingly common in recent years.[19] Here we limit our discussions to seed-mediated growth (or seeded growth) in a solution phase, in which metal atoms resulting from the reduction or decomposition of a precursor heterogeneously nucleate and then grow on the surface of seeds characterized by a single-crystal structure and well-controlled facets. The use of well-defined seeds allows us to systematically investigate the role(s) played by a thermodynamic or kinetic parameter in dictating their evolution into nanocrystals with different geometric shapes.

In the absence of presynthesized seeds (e.g., in a one-pot synthesis), the formation of colloidal metal nanocrystals in a solution phase can be divided into three major steps:[18a] (i) nucleation or formation of small clusters from metal atoms and ions; (ii) evolution of the nuclei into seeds with well-defined internal structures; and (iii) growth of the seeds into nanocrystals with distinctive shapes. The outcome is determined by a set of thermodynamic (e.g., reduction potential and surface capping) and kinetic (e.g., concentration, mass transport, temperature, and the involvement of foreign species) parameters that are intimately and intricately entangled to each other. In many cases, the type and number of nuclei or seeds formed in the early stage of a synthesis can be drastically changed when any one of the thermodynamic or kinetic parameters is altered, resulting in changes to the shapes taken by the final products. At the moment, it is still impossible to resolve and track alterations to the nuclei due to the lack of experimental tools capable of identifying and monitoring these structures that are consisted of a very small number of atoms and ions. As such, although a large number of different shapes have been obtained using one-pot syntheses, it has been difficult to understand why they are formed under a specific set of thermodynamic or kinetic conditions. Accordingly, it has been a grand challenge to single out and then investigate the explicit role played by a thermodynamic and kinetic parameter in controlling the shape evolution of metal nanocrystals in the setting of one-pot synthesis.

Different from one-pot synthesis, seeded growth, in which newly formed metal atoms are added onto the surface of preformed seeds,[20] allows us to better understand and control the shape of metal nanocrystals by avoiding the complicated, unknown nucleation process. Thanks to recent developments in electron microscopy and elemental mapping techniques, it is now feasible to resolve changes to the seeds due to growth by comparing the products sampled at different stages of a synthesis. Through the use of seeds with a well-defined internal structure, we could systematically examine the roles of various thermodynamic and kinetic parameters in controlling the evolution of seeds into nanocrystals exhibiting distinctive shapes. While our discussions can be applied to all types of seeds, here we mainly focus on those with a single-crystal structure and covered by a mix of low-index facets such as {111}, {110}, and {100}. As illustrated in this Perspective, this unique class of seeds can serve as a simple model system for the elucidation of mechanistic details involved in the evolution of colloidal metal nanocrystals into diversified shapes, as well as the development of experimental strategies for manipulating their shape evolution during a synthesis.

2. THERMODYNAMIC VERSUS KINETIC PRODUCTS

The syntheses of metal nanocrystals and organic compounds share many similarities, and yet marked by some key differences too. If we consider a synthesis of nanocrystals as a chemical reaction, the atoms derived from a precursor can be viewed as reactants while the nanocrystals with different shapes being products. Figure 1A shows a schematic illustration that is typically used in literature to explain the concept of thermodynamic versus kinetic control.[21] In this case, the product I (i.e., nanocrystals with shape I) is thermodynamically less stable relative to the product II (i.e., nanocrystals with shape II). However, the activation energy barrier (E_a) involved in the formation of product I is lower than that for the formation of product II. As such, product II is expected to be in dominance when the synthesis is conducted under thermodynamic control while product I will take over the dominance if the synthesis is switched to the condition of kinetic control. According to the Arrhenius equation (reaction rate = $A\,e^{-E_a/RT}$), the most effective way to reduce the impact of activation energy on reaction rate is to raise the reaction temperature. As a result, the simplest way to obtain thermodynamically and kinetically controlled products is to conduct the synthesis at relatively high and low temperatures, respectively.

It should be pointed out that the argument shown in Figure 1A only applies to the scenario where the nanocrystals with distinctive shapes correspond to the products of multiple parallel reactions. In reality, these nanocrystals may also correspond to the products of a set of sequential reactions. This represents a major difference between the syntheses of nanocrystals and organic compounds. While the different products of an organic synthesis often differ in chemical composition (except for those only involving isomerization), the differently shaped nanocrystals of a synthesis do share the same elemental composition. As a result, these nanocrystals can be better presented as the products of a set of sequential reactions, and it will be more appropriate to use the energy landscape in Figure 1B to illustrate the concept of thermodynamic versus kinetic control.[22] In general, we are supposed to obtain the thermodynamically controlled product with the global minimum in Gibbs free energy. During a synthesis, however, the product could be easily trapped in many
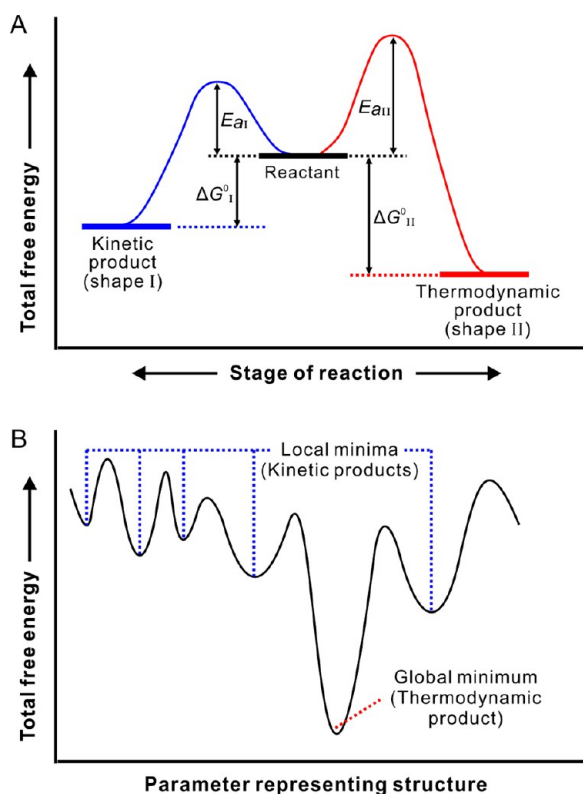
Figure 1. Schematic illustrations of two different scenarios of thermodynamic versus kinetic control that involve (A) two parallel reactions (B) a series of sequential reactions. In either case, the thermodynamic product, the one with the lower Gibbs free energy in (A) or the one at global minimum in (B), could be most conveniently accessed by raising the reaction temperature.

states (or shapes) corresponding to local minima when the synthesis is conducted under kinetically controlled conditions. Again, temperature plays the most important role in determining whether thermodynamic or kinetic control is in dominance. In this case, one has to conduct the synthesis at relatively low and high temperatures, respectively, in order to generate kinetically and thermodynamically controlled products. It is also interesting to point out that thermodynamic control only cares about the final state, not the process, whereas kinetic control is all about the exact process.

3. THERMODYNAMIC CONTROL

The essence of thermodynamic control is to give a system an adequately long period of time so that all the atoms can reach their final destinations to attain the global minimum for the Gibbs free energy of the entire system. This can be accomplished by aging the sample for a long period of time, raising the temperature of a system to increase the mobility of atoms on the surface, or both. The shape obtained under thermodynamic control can be considered as an *equilibrium state* defined by a set of experimental parameters, including temperature, pressure, and surrounding environment. As such, whenever there is a perturbation to any one of these parameters, the state and thus the shape will be altered accordingly.

3.1. Equilibrium Shape of a Nanocrystal in a Vacuum. A nanocrystal will take its equilibrium shape when its total Gibbs free energy reaches the global minimum.[23] As shown in eq 1, the total Gibbs free energy of a nanocrystal can be expressed as the sum of Gibbs free energy for the bulk and the excess Gibbs free energy caused by the surface:

$$dG = dG_{bulk} + \gamma \, dA \tag{1}$$

where γ denotes the specific surface free energy (per unit area) and A is the surface area. At a fixed volume, the total Gibbs free energy will reach the minimum value under the condition of a minimized total surface free energy:

$$\int \gamma_i \, dA_i = \text{minimum} \tag{2}$$

where the integral is taken over the entire surface of a nanocrystal. This equation implies that a nanocrystal should take an equilibrium shape when its total surface free energy is minimized. If the specific surface free energy does not depend on the direction, as in an isotropic system like a noncrystalline material (a liquid or an amorphous solid), the total surface free energy is solely proportional to the total surface area. In this case, the total surface free energy will be minimized when the "nanocrystal" (or, more appropriately, "nanoparticle" because of the amorphous structure in this case) takes a spherical shape to minimize the total surface area at a fixed volume. For a crystalline material, however, the surface free energies of different crystallographic planes tend to differ from each other because of the intrinsic anisotropy in atomic arrangement. As a result, one has to know the specific surface free energies of different crystallographic planes in order to derive the equilibrium shape of a nanocrystal in a vacuum.

The specific surface free energy is defined as the increase in free energy per unit area when a new surface is created. When atoms are tightly bound to each other, the bonds between them need to be broken in order to create a pair of new surfaces. In a sense, the surface free energy reflects the cost in energy when bonds are broken and is thus determined by the number and strength of bonds involved. Specifically, under the *broken bond approximation* where only interactions between the nearest neighbors are considered, the specific surface free energy of a crystallographic plane can be calculated using the following equation:

$$\gamma = \frac{1}{2} N_B \varepsilon \rho_A \tag{3}$$

where N_B is the number of broken bonds per surface unit cell (or per surface atom), ε is the bond strength, ρ_A is the number of surface atoms per unit area, and the factor $^1/_2$ is used because each bond involves two atoms.[24] Both N_B and ρ_A can be derived from the crystal structure. Figure 2 schematically illustrates the models of three principal low-index planes, (111), (100), and (110), of a face-centered cubic (fcc) metal with a lattice constant of a_0. The dashed box in each model represents the corresponding unit cell for the surface atoms. From these models, the values of ρ_A are calculated as $2.31(1/a_0^2)$, $2(1/a_0^2)$, and $1.41(1/a_0^2)$ for the (111), (100), and (110) planes, respectively. In addition, the number of broken bonds per surface unit cell can be easily derived as 3 and 4 for the (111) and (100) planes, respectively. In the case of the (110) plane, it should be noted that one additional broken bond from the subsurface (labeled as $a'b'$) needs to be included because it is also involved in the formation of two (110)-type surfaces. Consequently, the number of broken bonds per surface unit cell is 6 instead of 5 for the (110) plane.

Once N_B and ρ_A have been determined, the specific surface free energies of these low-index planes can be calculated as
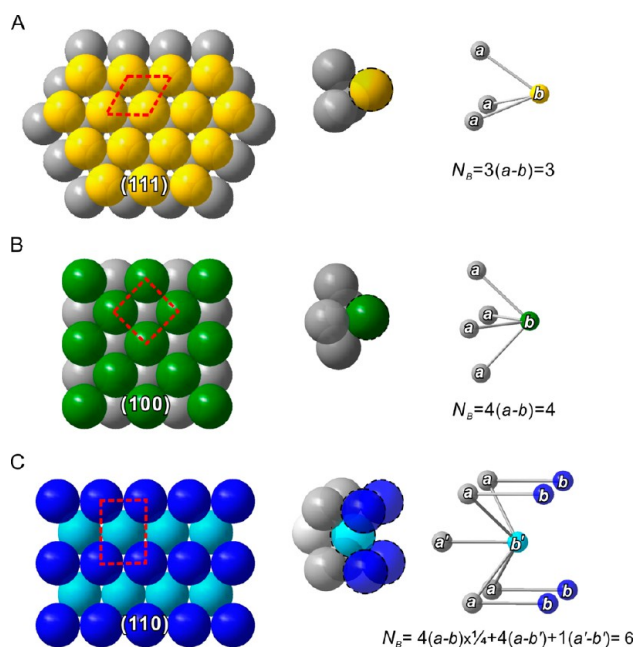
Figure 2. Models of the three major low-index planes in a face-centered-cubic metal and the corresponding numbers of bonds per surface unit cell (N_B) that have to be broken in creating a pair of new surfaces: (A) (111), (B) (100), and (C) (110). The red dashed box represents the surface unit cell for each crystallographic plane.

$\gamma_{(111)} = 3.46(\varepsilon/a_0^2)$, $\gamma_{(100)} = 4(\varepsilon/a_0^2)$, and $\gamma_{(110)} = 4.24(\varepsilon/a_0^2)$. These results indicate that the surface free energies of the low-index planes of an fcc metal increase in the order of $\gamma_{(111)} < \gamma_{(100)} < \gamma_{(110)}$. These results also imply that for an fcc metal, the anisotropy ratio between the surface energies of an arbitrary crystallographic plane and the (111) plane should be the same regardless of its elemental composition. The *broken bond approximation* offers a simple method for estimating the surface free energies of a metal nanocrystal surrounded by vacuum. However, the exclusion of some other factors such as the interactions with the second and the third nearest neighbors and the relaxation of surface could potentially lead to significant errors in calculating the surface free energies of different types of crystallographic planes, especially for those with high indices.[25] Alternatively, computational modeling based on density functional theory (DFT) offers a more accurate approach to the calculation of surface free energies.[26] It was shown that the ratio between the surface energies of an arbitrary plane and the (111) plane can indeed differ slightly between different metals.

For a metal nanocrystal, its equilibrium shape cannot be spherical because many high-index facets with relatively high specific surface free energies would be required for the formation of a perfect sphere. When considering a nanocrystal made of an fcc metal and situated in a vacuum, one would expect an octahedral or tetrahedral shape so that only {111} facets with the lowest specific surface free energy will be exposed on the surface. Both octahedron and tetrahedron, however, have larger surface area-to-volume ratios when compared with a cube enclosed by {100} facets. In an effort to minimize the total surface free energy, a "hybrid" shape enclosed by a mix of {100} and {111} facets in the right proportion eventually becomes the winner favored by thermodynamics.

Theoretically, the equilibrium shape of a nanocrystal in a vacuum can be derived using the Wulff construction.[27] The basic principle is shown in eq 4,

$$\frac{\gamma_i}{h_i} = \text{constant} \tag{4}$$

where γ_i and h_i are the specific surface free energy and the distance to the center for the ith facet, respectively. This equation indicates that the distance of the facet from the center of the crystal is proportional to the specific surface free energy of a given facet. Following this theorem, the Wulff construction begins with a polar plot of the specific surface free energies (γ_i) as a function of orientation, where the length of each radius vector (h_i) is proportional to its specific surface free energy (γ_i). Next, a line perpendicular to each vector is drawn at the intersection point with the polar plot, as represented by the short-dashed lines in Figure 3A. Repeating the procedure for all
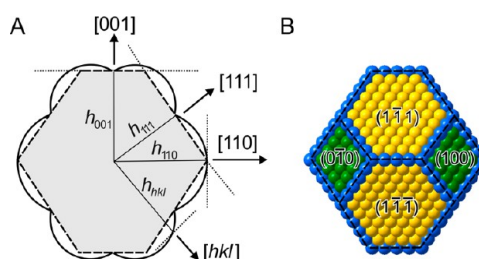
Figure 3. (A) Two-dimensional section of a polar plot of the specific surface free energies of an fcc crystal oriented along $[1\bar{1}0]$ as derived from the Wulff thereom. The inner envelope denoted by dashed lines corresponds to the equilibrium shape of the nanocrystal. (B) Three-dimensional atomic model corresponding to the equilibrium shape shown in (A).

different directions represented by the crystal axes eventually results in a closed polyhedron inside the polar plot, which represents the equilibrium shape of the nanocrystal. In principle, one can always predict the equilibrium shape (i.e., the so-called Wulff shape) of a metal once the specific surface free energies of different crystallographic planes become available either theoretically[26] or experimentally.[28]

Figure 3A shows a 2-D polar plot of the specific surface free energy and the corresponding equilibrium shape of an fcc nanocrystal viewed along $[1\bar{1}0]$. In the 3-D space, this equilibrium shape corresponds to a truncated octahedron, with only {100} and {111} facets on the surface. Based on the *broken bond approximation* for an fcc metal, its {111} facets are lower in specific surface free energy than its {100} facets, with the ratio of $\gamma_{(100)}$ to $\gamma_{(111)}$ being 1.16. As a result, it is anticipated that the {111} facets will take a slightly larger proportion than the {100} facets according to the Wulff theorem. Taken together, the equilibrium shape of a nanocrystal made of an fcc metal and surrounded by a vacuum should be a truncated octahedron (Figure 3B), where the ratio between the areas of {100} and {111} facets can vary slightly depending on the metal.

When a single-crystal seed made of an fcc metal is allowed to grow in a vacuum and truly under thermodynamic control, it should evolve into a truncated octahedron with increasingly larger sizes, as confined by the Wulff theorem. Since the equilibrium shape of a nanocrystal is determined by the relative magnitudes of specific surface free energies associated with different crystallographic facets, it is feasible to alter the ratios

between the specific surface free energies to obtain nanocrystals with shapes other than the one predicted using the Wulff theorem. How to manipulate the relative specific surface free energies associated with different crystallographic planes has been a central theme in engineering the shape of metal nanocrystals formed under thermodynamic control. Among the various approaches in this endeavor, surface adsorption of chemical species (atomic, ionic, molecular, or macromolecular) from a gas or solution phase seems to be the simplest and most versatile.

3.2. Equilibrium Shape of a Nanocrystal in a Gas Phase in the Presence of an Adsorbate.

In heterogeneous catalysis, it has been documented by many reports that the gas molecules can chemisorb onto the surface of a nanocrystal via covalent bonding and thus effectively reduce the specific surface free energy.[29] Due to the involvement of covalent bonding, the adsorbate can preferentially bind only to a specific type of facet on the surface and thus alter the ratios between the specific surface free energies of different facets, leading to the formation of nanocrystals with profiles deviated from the Wulff shape predicted for the same system in a vacuum.

In a study reported in 1985, for example, Pt nanocrystals supported on an amorphous SiO_2 substrate were found to change shape when the sample was annealed at 600 °C in the presence of different gas molecules (Figure 4A,B).[30] The equilibrium shapes observed for the Pt nanocrystals were truncated cuboctahedrons and cubes when the samples were annealed in N_2 and H_2, respectively. Interestingly, the Pt nanocrystals could be reversibly switched between these two
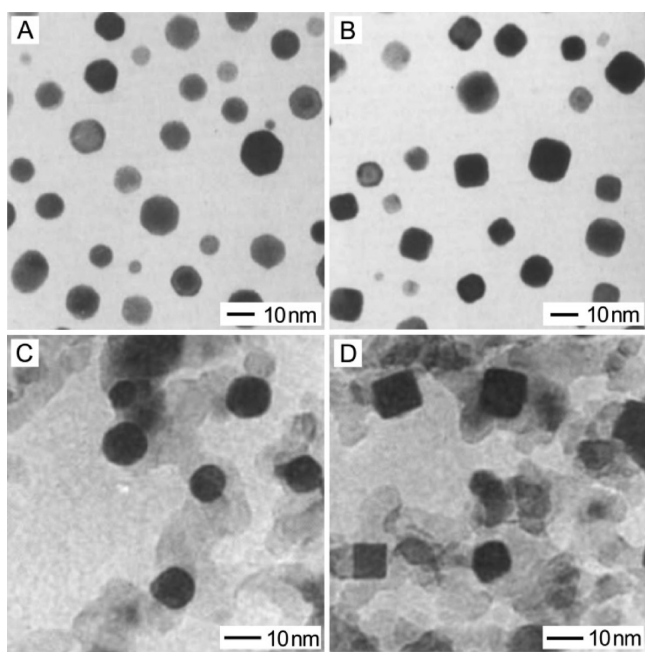

Figure 4. Transformations between Pt nanocrystals with distinct shapes when they were thermally annealed under different gas atmospheres. (A,B) TEM images of Pt nanocrystals supported on planar amorphous SiO_2 after annealing under (A) N_2 and (B) H_2 at 600 °C for 24 h. (Adapted with permission from ref 30. Copyright 1985 Elsevier B.V.) (C,D) TEM images of Pt nanocrystals supported on Al_2O_3 powders after annealing (C) in air at 700 °C for 1 h and (D) under H_2 containing a trace amount of H_2S at 500 °C for 16 h. (Adapted with permission from ref 32. Copyright 1986 Nature Publishing Group.)

shapes by alternating the gas under which the sample was thermally annealed. Even though the exact mechanism for the shape transformation was not clear at that time, this study demonstrated the feasibility to control the shape of a metal nanocrystal by exposing the sample to an appropriate gas. At an elevated temperature, the migration of atoms on the surface would be greatly accelerated, allowing the nanocrystal to quickly attain the equilibrium shape defined by a new set of thermodynamic parameters.[31]

A similar observation was reported in 1986 for Pt nanocrystals supported on Al_2O_3 powders when the sample was subjected to thermal annealing under different gaseous environments.[32] As shown in Figure 4C,D, annealing the nanocrystals in air led to a nearly spherical shape, whereas a cubic shape was obtained in a H_2 atmosphere containing a trace amount of H_2S. If the interaction between the gas molecules and Pt surface is relatively weak, as in the case of air where only physisorption was involved, the relative surface energies for different types of facets of a nanocrystal are more or less equivalent to the case of vacuum. As such, it is understandable that the nanocrystal would take a nearly spherical shape similar to what is predicted using the Wulff theorem. In contrast, the presence of sulfur species would induced the formation of a cubic shape, which can be attributed to the sulfur poisoning mechanism commonly observed for noble-metal catalysts.[33] In this case, the preferential binding of sulfur to Pt(100) could effectively lower its specific surface free energy to reverse the order of relative specific surface free energies between $\gamma_{(100)}$ and $\gamma_{(111)}$. In maximizing the expression of the facet favored by thermodynamics, the Pt nanocrystals were transformed into a cubic shape enclosed by six {100} facets as long as there was an adequate amount of H_2S in the gaseous environment.

Taken together, the above two examples demonstrated that the shape of a metal nanocrystal supported on a solid substrate can be altered in a controllable fashion by introducing a gaseous species capable of covalently binding to a specific type of facet. The chemisorption will lower the specific surface free energy of that facet and thereby alter the ratios between the areas occupied by different types of facets on the surface of a nanocrystal. Despite these successful demonstrations, the use of a high temperature and a solid support, as well as the limited choices of gases, may greatly limit the potential application of such a gas-phase method for engineering the shape of metal nanocrystals. When switching to a solution-phase method, there would be no such limitation due to the availability of many different capping agents for each type of facet.

3.3. Equilibrium Shape of a Nanocrystal in a Solution in the Presence of a Capping Agent.

Capping agents are ionic species, small molecules, or macromolecules that can selectively bind to different types of facets on a nanocrystal to alter their specific surface free energies and thus their proportions in terms of area.[18,34] When a capping agent is introduced into a reaction solution, the type of facet stabilized by the capping agent will exhibit a lower specific surface free energy, leading to the formation of nanocrystals with a shape that maximizes the expression of that type of facet. In addition to the Wulff theorem, the shape taken by a growing nanocrystal can also be understood from a kinetic perspective on the basis of the relative growth rates of different crystallographic planes. Since the capping agent chemisorbed on a facet will hinder or prevent the deposition of atoms onto this facet, surface capping will eventually lead to the formation of a shape with that particular facet preferentially expressed. In other words, the
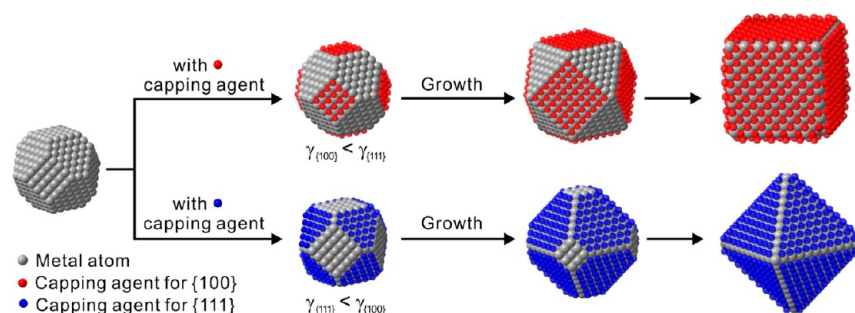
Figure 5. Schematic illustrations showing the role of capping agents in directing the growth of a single-crystal seed made of an fcc metal. The shape of resultant nanocrystals can be manipulated in a controllable fashion through the introduction of a capping agent (represented by red or blue dots) that can selectively bind to a specific type of facet, altering the order of surface free energies and eventually leading to the formation of a nanocube enclosed by {100} facets and an octahedron enclosed by {111} facets, respectively.

facet covered by the capping agent will take a slower growth rate and thus a greater proportion on the surface. Taking the growth of a truncated octahedral seed as an example, Figure 5 compares the pathways of shape evolution in the presence of two complementary capping agents. With the introduction a capping agent for the {100} facets, the order of surface free energies will become $\gamma_{\{100\}} < \gamma_{\{111\}}$, and thereby the growth will be faster along the $\langle 111 \rangle$ directions than along the $\langle 100 \rangle$ directions. Owing to the difference in growth rate, the ratio between the areas of {100} and {111} facets on the surface will gradually increase, and the nanocrystal will evolve from truncated octahedron to cuboctahedron, truncated cube, and eventually a cube enclosed by {100} facets only. In contrast, the specific surface free energy of {111} facets will be further lowered in the presence of a capping agent for the {111} facets. The faster growth rate along the $\langle 100 \rangle$ directions will keep reducing the proportion of {100} facets during growth, eventually leading to the formation of an octahedron enclosed by {111} facets only.

Thanks to the availability of a rich variety of chemicals that can act as capping agents for different types of surfaces, solution-phase synthesis provides a powerful route to the preparation of metal nanocrystals with a myriad of shapes. Generally, the preferential binding of a capping agent to a specific metal surface may be attributed to many factors, including the crystal structure and the functional group(s) of a capping agent, as well as the electronic and surface structure of the metal. It is possible to calculate the binding energies of a chemical species to a metal surface through a computational approach based on DFT and *ab initio* calculations. In one study, the binding of poly(vinylpyrrolidone) (PVP) to different types of Ag surfaces were studied using DFT calculation, where the repeating unit of PVP was represented by ethane and 2-pyrrolidone (2P).[35] Since ethane is an inert and nonpolar species, its interaction with a Ag surface should only involve van der Waals (vdW) attraction. In contrast, the oxygen and possibly nitrogen atoms in the 2P ring can form much stronger chemical bonds with a Ag surface, as illustrated in Figure 6A. This study suggests that both interactions, including vdW and covalent bonding, need to be taken into consideration during the calculation in order to compare the total binding energies. The calculation results indicate that binding of PVP to Ag(100) is stronger than to Ag(111), in agreement with experimental observations reported in a number of earlier studies.[36] Interestingly, when considering the entire chain of a PVP macromolecule, its preference of binding to Ag(100) over
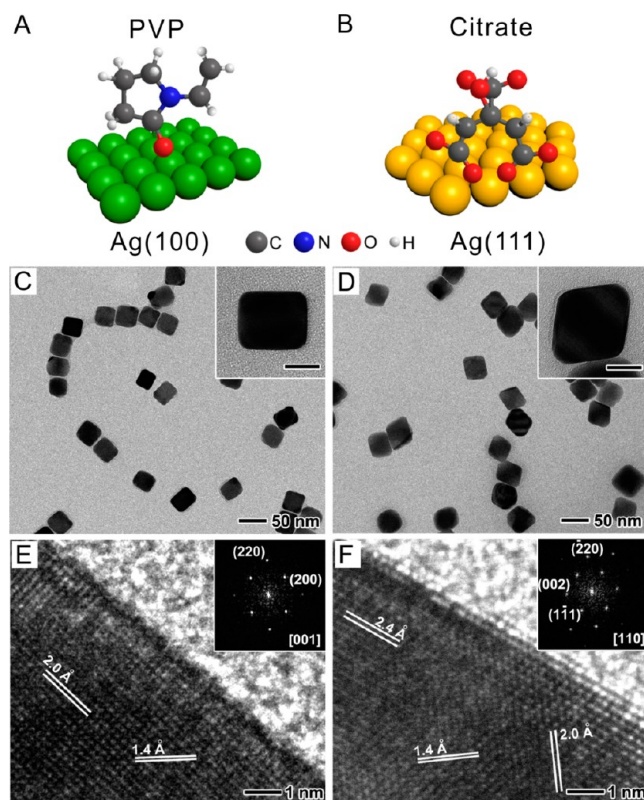
Figure 6. Schematic illustrations of the adsorption of (A) a repeating unit of PVP and (B) a citrate ion on Ag(100) and Ag(111) surfaces, respectively. (Reproduced with permission from ref 58. Copyright 2012 American Chemical Society.) (C,D) TEM images of Ag nanocrystals that were grown from single-crystal, spherical Ag seeds in the presence of (C) PVP and (D) sodium citrate, respectively, as the capping agents. The insets show TEM images of individual nanocrystals taken from the same samples at a higher magnification (scale bar: 20 nm). (E,F) High-resolution TEM images taken from the edge of an individual (E) nanocube and (F) octahedron. The insets show the corresponding selected area electron diffraction patterns, confirming the expressions of {100} and {111} facets on the surfaces of the nanocube and octahedron, respectively. (Reproduced with permission from ref 39. Copyright 2010 American Chemical Society.)

Ag(111) was found to increase exponentially with the number of repeating units.

Complementary to PVP, citrate is a capping agent commonly used for the synthesis of Ag nanocrystals enclosed by {111} facets.[37] The binding energies of citrate ions to different types
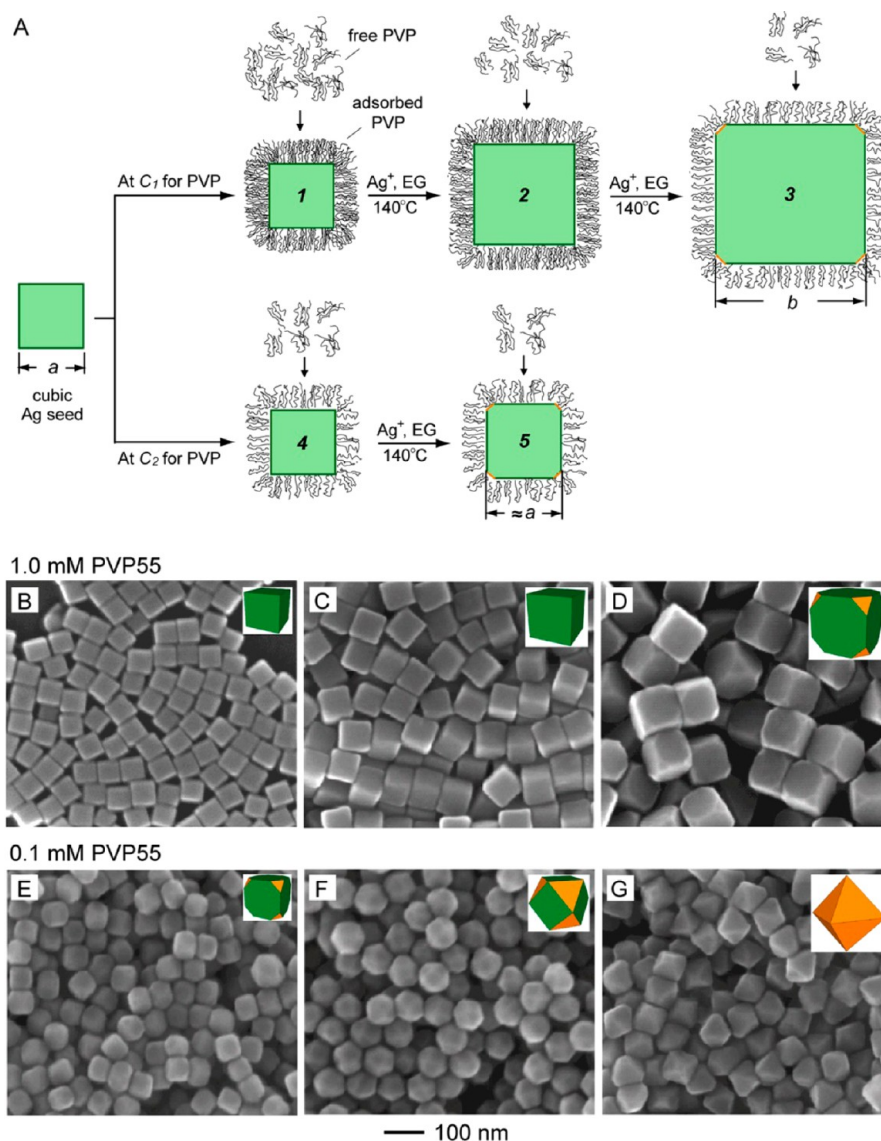
Figure 7. (A) Schematic illustration showing the growth of a Ag cubic seed with an edge length of *a* nm in the presence of PVP at a high concentration C_1 and a critically low concentration C_2 ($C_1 > C_2$). (B−G) SEM images of Ag polyhedrons obtained from 40 nm cubic seeds in the presence of (B−D) 1.0 mM and (E−G) 0.1 mM PVP55. The samples were collected at different stages of the seeded growth: (B,E) 5 min, (C,F) 10 min, and (D,G) 20 min. The insets show the corresponding models of the polyhedrons. (Reproduced with permission from ref 36d. Copyright 2012 American Chemical Society.)

of Ag surfaces have been calculated using *ab initio* DFT, and the results indicate that the binding energy is highly sensitive to the symmetry matching between citrate ion and the metal surface.[38] Whereas a citrate ion has a pseudo-three-fold rotational axis, the Ag(100) surface is characterized by four-fold rotational symmetry due to square packing. As a result of mismatch in both symmetry and interatomic distance, only two Ag−O bonds can be formed between a citrate ion and the Ag(100) surface, resulting in a binding energy of 3.69 kcal/mol. In comparison, as shown in Figure 6B for Ag(111) surface with hexagonal packing, the citrate ion and surface atoms are well-matched in terms of symmetry and interatomic distance. For each citrate ion, it can form four Ag−O bonds with Ag(111) surface, resulting in a much higher binding energy of 13.84 kcal/mol. The 10 kcal/mol difference in binding energy implies that the binding constants of citrate ion toward the Ag(111) on Ag(100) surfaces differ by six orders in magnitude.

The orthogonal binding of PVP and citrate to Ag(100) and Ag(111) surfaces, respectively, makes them ideal candidates of capping agents for the exclusive formation of Ag nanocrystals enclosed by {100} and {111} facets. Figure 6C−F shows an experimental demonstration that involves the use of single-crystal, nearly spherical Ag nanocrystals as seeds, whose surfaces are covered by a mix of {111} and {100} facets.[39] To single out the explicit role played by a capping agent in controlling the shape of Ag nanocrystals, all other experimental parameters were kept the same, except for the use of a different capping agent. As anticipated, the use of PVP that selectively binds to Ag(100) surface resulted in the formation of Ag cubes only (Figure 6C). The surface of such a cube was mainly covered by {100} facets, as supported by the high-resolution TEM image in Figure 6E. In contrast, as shown by the TEM and high-resolution TEM images in Figure 6D,F, Ag octahedrons enclosed by {111} facets were obtained as the only product when the PVP was replaced by sodium citrate.

Taken together, an integration of computational and experimental studies will offer a powerful and irreplaceable approach to revealing the role played by a capping agent in carving out the shape of a nanocrystals at a atomic/molecular level, as well as to the identification of capping agent(s) for generating a specific type of metal surface. In principle, such a thermodynamic control, as enabled by the introduction of a capping agent to selectively bind to a specific type of metal surface, allows people to effectively manipulate the order of specific surface free energies and ultimately obtain colloidal nanocrystals with well-controlled shapes or facets.

3.4. Quantitative Analysis of the Coverage Density of a Capping Agent.

Although a large number of capping agents have been demonstrated for generating colloidal metal nanocrystals with various shapes,[34] their coverage densities on the surfaces of nanocrystals are often unknown. As a result, an excess amount of the capping agent has to be introduced into a synthesis to ensure effective passivation of the newly formed surface as the nanocrystals grow into larger sizes. We have recently started to address this issue by experimentally measuring the coverage density of a capping agent on the surface of colloidal nanocrystals. In one study, we designed a set of experiments to quantitatively analyze the role played by the concentration of PVP in the growth of Ag nanocubes into larger nanocrystals.[36d] The experiments involved the use of Ag nanocubes as seeds in ethylene glycol at an elevated temperature, with $AgNO_3$ serving as a precursor to Ag and PVP of different initial concentrations as a capping agent. The cubic seeds could evolve into well-defined polyhedrons ranging from cubes (with enlarged sizes relative to the initial seeds) to truncated cubes, cuboctahedrons, truncated octahedrons, and octahedrons depending on the initial concentration of PVP involved. We could derive the coverage density of PVP on Ag(100) surface by combining the results from two parallel experiments (Figure 7). In the first experiment, we followed the growth of Ag nanocube at a fixed initial concentration of C_1 for PVP and determined the size of the corresponding cubes, at which {111} facets started to appear at the corner sites. In the second experiment, the same batch of Ag nanocubes were allowed to grow at a set of decreasing initial concentrations for PVP to figure out the critical initial concentration C_2, at which {111} facets would start to appear at the corner sites from the very beginning of a synthesis. We then calculated the coverage density of PVP on Ag(100) from the differences in concentration ($C_1 - C_2$) and total surface area of Ag cubes between these two samples. The coverage density was found to be 140 and 30 repeating units per nm^2 for PVP of 55 000 and 10 000 g/mol in molecular weight, respectively, for cubic seeds of 40 nm edge length. These values dropped slightly to 100 and 20 repeating units per nm^2, respectively, when Ag cubes of 100 nm edge length were employed as the seeds.

We have also demonstrated a different approach for quantitatively analyzing the role played by Br^- ions in controlling the shape of Pd nanocrystals through a combination of X-ray photoelectron spectroscopy (XPS) and inductively coupled plasma mass spectroscopy (ICP-MS).[40] We first prepared Pd cubes with three different edge lengths (7.5, 10.5, and 18.0 nm) by reducing Na_2PdCl_4 with ascorbic acid in the presence of Br^- ions as a capping agent for Pd(100) surface. After extensive washing with water, the samples were dissolved with concentrated nitric acid and analyzed by ICP-MS. Thanks to the ultrahigh sensitivity of ICP-MS, the atomic ratio of Br^- to Pd could be directly obtained, and then the atomic ratio of

Br^- to surface Pd could be calculated on the basis of the dimensions of the Pd cubes. The ratios of Br^- to surface Pd atoms for these three samples were found to be more or less the same, giving a value of approximately 0.8. This number suggests the formation of roughly a monolayer of Br^- ions on the surface of each Pd cube, with a coverage density of about 10 Br^- ions per nm^2. The chemisorption of Br^- ions was also validated by XPS analysis and we observed changes to the electronic structure of the surface of Pd cubes due to the transfer of electrons between the chemisorbed Br^- ions and the Pd atoms on the surface. As a matter of fact, the Pd atoms on the surface were shown by XPS to have an oxidation state of +2.

The quantitative information about the surface coverage density of a capping agent allows us to experimentally design a shape-control synthesis by minimizing the amount of Br^- ions added into a reaction system. The essence of this study is illustrated in Figure 8A. A control experiment without using
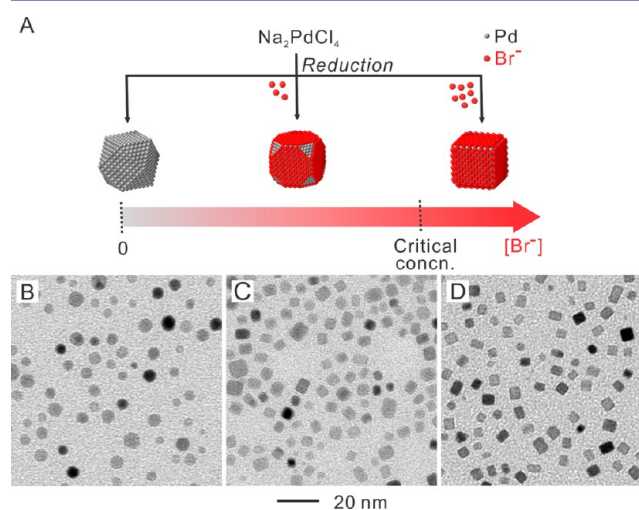
Figure 8. (A) Schematic showing how the shape of a Pd nanocrystal can be controlled by adding a specific amount of Br^- ions into the solution as a capping agent for the Pd(100) surface. (B–D) TEM images of Pd nanocrystals synthesized at different amounts of Br^- ions: (B) with no Br^- ions added, (C) with the addition of inadequate Br^- ions, and (D) with the addition of adequate Br^- ions. Three distinctive shapes for the as-synthesized Pd nanocrystals were clearly observed: (B) cuboctahedral, (C) truncated cubic, and (D) cubic. (Adapted with permission from ref 40. Copyright 2013 American Chemical Society.)

any KBr yielded nearly spherical Pd nanocrystals enclosed by a mix of {100} and {111} facets because of the lack of a capping agent for the Pd(100) surface (Figure 8B). The total surface area of Pd nanocrystals synthesized under this condition can be calculated on the basis of the particle size. Next, the minimum amount of Br^- ions needed to cover the entire Pd(100) surface can be derived from a set of parameters, including the amount of Pd precursor, the conversion percentage of Pd precursor, and the coverage density of Br^- ions on Pd(100) surface. Based on this information, we can simply design a new synthesis by just adding the necessary amount of Br^- ions into the reaction system. As shown in Figure 8C, Pd truncated nanocubes were obtained when an inadequate amount of Br^- was introduced, where the number of Br^- ions was too low to passivate all the exposed Pd(100) surface, leading to the expression of a small portion of {111} facets on the surface. In comparison, with the
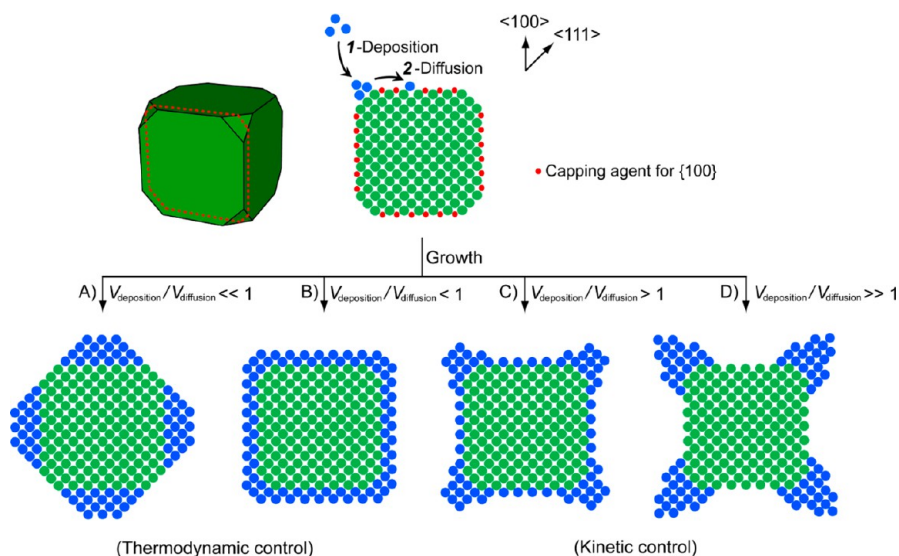
Figure 9. Schematic illustrations showing the shape evolution of a cubic seed with side faces being covered by a capping agent under four different kinetic conditions. The 2-D atomic models correspond to the cross-section (dashed red line) in the 3-D model.

introduction of an adequate amount of Br^- ions, we obtained well-defined Pd cubes enclosed by {100} facets (Figure 8D). These results suggest that the exact shape of nanocrystals (in the case of Pd cubes, the degree of corner truncation) can be fine-tuned by adjusting the amount of a capping agent introduced into a synthesis.

Overall, thermodynamic control in solution phase is a simple and yet effective strategy that can be easily implemented during an experiment. As a result, it has been widely explored for the shape-controlled synthesis of colloidal metal nanocrystals. A thermodynamically controlled synthesis can be implemented in two slightly different ways: (i) introducing different types of capping agents to selectively chemisorb onto different types of metal surfaces and thus lower the specific surface free energies of these facets and (ii) controlling the coverage density of a capping agent by adjusting its concentration in the reaction solution to manipulate its power in lowering the specific surface free energy of a facet. Thanks to the efforts from many research groups, a variety of capping agents other than PVP, citrate, and Br^- ions have been identified over the past decade for the shape-controlled synthesis of colloidal metal nanocrystals. To this end, I^- ions have been established as an effective capping agent for Pd(100) and Au(111) surfaces,[41] and CO has been demonstrated with selectivity toward Pt(100)[42] and Pd(111)[43] surfaces. In addition, some biological molecules/macromolecules such as peptides and RNAs have been shown with a capability to selectively bind to different types of metal surfaces and thereby induce the formation metal nanocrystals with different shapes.[44] Most significantly, the biomolecules can be rationally designed with different functional groups to selectively bind to specific metal surfaces, synthesized, and then employed as capping agents. Through the use of some existing analytic tools, it is even feasible to measure and compare the binding affinities between the biomolecules and various metal surfaces.[44d,e]

3.5. Notes on Thermodynamic Control and Capping Agent. Although remarkable progress has been made in thermodynamically controlled synthesis of colloidal metal nanocrystals with well-defined facets, there are still a number of challenges or barriers. First of all, there is essentially no report on capping agents capable of preferentially stabilizing high-index facets of a metal nanocrystal. Because of their high densities of low-coordination sites, high-index facets are generally considered to have better performance in many catalytic reactions. A facile protocol for preparing colloidal metal nanocrystals enclosed by high-index facets would be highly desirable. Crystallographic planes of high Miller index are not flat on an atomic scale. They are typically comprised of narrow, low-index planes separated by steps of one atomic high. Some of the capping agents developed for low-index facets may still apply to high-index facets, as long as the atomic steps can also be somehow stabilized. Future effort needs to be directed toward the identification of capping agents for high-index facets. On the other hand, owing to the high symmetry of their lattices, the surface of a metal nanocrystal is typically represented by multiple equivalent sites that could not be differentiated by thermodynamic means. For example, all of the six {100} facets of a nanocrystals made of an fcc metal should be exactly identical in terms of atomic arrangement and specific surface free energy. As a result, it is impossible to synthesize nanocrystals with asymmetric shapes or structures under thermodynamic control. A combination with other strategies, such as kinetic control, is necessary in order to overcome the limitation of thermodynamically controlled synthesis and thus generate metal nanocrystals with novel shapes and structures.

It is also worth noting that the relatively large physical dimensions of a polymer-based capping agent may compromise its role when nanocrystals with very small sizes are involved. For example, PVP is no longer effective in capping the {100} facets to generate Ag cubes with edge lengths shorter than 30 nm. In contrast, the much smaller size of Br^- ions make them well-suited for capping the {100} facets on Ag cubes or rectangular bars with dimensions smaller than 30 nm.[45] Our preliminary study indicates that Br^- ions can likely passivate the {100} facets of Ag cubes with edge lengths down to a length scale below 10 nm. On the other hand, Br^- ions have also been widely used as a capping agent with specificity toward {100} facets for a number of other noble metals such as Pd,[46] Pt,[47] and Rh.[48] A typical protocol for the synthesis of noble-metal nanocrystals covered by {100} facets involves the reduction of a

salt precursor in an aqueous or polyol system containing Br^- ions, a salt precursor (which may contain Br^- ions in some cases), a reducing agent, and a colloidal stabilizer (often, PVP). Depending on the twin structure of seeds formed in the nucleation step, a variety of nanocrystals enclosed by {100} facets have been successfully synthesized, including cubes, right bipyramids, and pentagonal rods or wires. For Pt nanocubes, in particular, they could be prepared with an edge length as short as 4 nm.[47b]

4. KINETIC CONTROL

4.1. Mechanistic Understanding of Kinetic Control. As driven by thermodynamics, the atoms initially added to a specific region on the surface of a nanocrystal (typically, the most active site with the highest surface free energy) should migrate to the site lowest in surface free energy. In many cases, however, the surface diffusion is not adequate so the nanocrystal will be trapped in a thermodynamically less favorable shape (like one of the local minima shown in Figure 1B), leading to the formation of a kinetic product. To this end, the exact shape (or morphology) displayed by the nanocrystal will be determined by the relative magnitudes of the rates corresponding to atom deposition ($V_{deposition}$) and surface diffusion ($V_{diffusion}$). Both of them are kinetic parameters and can be manipulated by varying experimental conditions related to chemical kinetics.

Taking the growth of a cubic seed (with all of its six side faces being completely covered by a capping agent) as an example, the newly formed atoms should be deposited onto the corners owing to the high energy of these sites (Figure 9). Upon deposition, the adatoms can have two different options: staying at the corner sites where deposition occurs or migrating to different sites (e.g., edges and side faces) through surface diffusion. The growth pathway of this cubic seed and thereby the shape taken by the product have a strong dependence on the ratio between the rates for atom deposition and surface diffusion (i.e., $V_{deposition}/V_{diffusion}$). When $V_{deposition}/V_{diffusion} \ll 1$, most of the adatoms at the corners will migrate to edges and side faces and the growth will prevail along the ⟨100⟩ and ⟨110⟩ directions, leading to the formation of cuboctahedrons favored by thermodynamics (Figure 9A). When $V_{deposition}/V_{diffusion} \gg 1$, on the contrary, surface diffusion can be ignored and the growth will be switched to the ⟨111⟩ directions, promoting the formation of a kinetically favored octapod as the product (Figure 9D). Similar arguments can also be applied to the situations where the ratios of $V_{deposition}$ to $V_{diffusion}$ are situated between the two extremes. For instance, when $V_{deposition}/V_{diffusion}$ is slightly less than 1, some of the adatoms will stay at the corners whereas the rest can diffuse to the edges and side faces, leading to the formation of an enlarged cube with slightly truncated corners (Figure 9B). This shape is also favored by thermodynamics as long as there is enough capping agent in the reaction solution to effectively passivate and thus stabilize the enlarged side faces. When $V_{deposition}/V_{diffusion}$ is slightly greater than one, a small portion of the adatoms at the corners can migrate to the edges (which are relatively more reactive than the side faces due to a lower coverage density for the capping agent). As a result, the product will become a concave cube (Figure 9C). It is worth pointing out that the total surface free energies of these four different types of nanocrystals are expected to increase in the order of cuboctahedron < truncated cube < concave cube < octapod. It is worth pointing out that the surface diffusion rate can serve as a reference point to

determine if the product is formed under thermodynamic or kinetic control. When $V_{deposition}/V_{diffusion} < 1$, the synthesis is under thermodynamic control, and vice versa, the synthesis is under kinetic control when $V_{deposition}/V_{diffusion} > 1$.

Significantly, both $V_{deposition}$ and $V_{diffusion}$ can be varied experimentally in a well-controlled fashion. In general, $V_{deposition}$ has a direct correlation with the rate at which the newly formed metal atoms are supplied. This rate is largely determined by the reduction rate (V) of a salt precursor (A) by a reductant (B). In an ideal reaction situation (without the involvement of intermediate steps), V can be expressed as eq 5:[49]

$$V = k[A]^x[B]^y \tag{5}$$

where [A] and [B] are the molar concentrations of A and B, respectively; exponents x and y are the reaction orders with respect to A and B; and k is the rate constant of the reduction reaction that has a strong dependence on temperature. As a result, $V_{deposition}$ can be manipulated in a number of ways, including variations of reagent concentration and reaction temperature, the choice of a specific type of reductant or precursor, and the type of coordination ligand for the metal ion. Among them, controlling the injection rate of the precursor solution (typically, the precursor) with the use of a syringe pump has been demonstrated to be a simple and effective method for controlling the reagent concentration, and thus the magnitude of $V_{deposition}$.[50]

Surface diffusion is a thermally activated process that involves the motion of adatoms on a solid surface through a jumping or hopping mechanism.[51] The diffusion coefficient D that measures the rate of jumping of an adatom across a surface can be expressed as an Arrhenius-type equation:

$$D = D_0 \exp(-E_{diff}/RT) \tag{6}$$

where D_0 is the diffusion pre-exponential factor, E_{diff} is the potential energy barrier to diffusion, R is the ideal gas constant, and T is the absolute temperature. Clearly, for surface diffusion of adatoms across the surface of a growing seed, D and thus $V_{diffusion}$ are mainly determined by the reaction temperature (T) and E_{diff}. In general, E_{diff} is determined by a number of factors, including the strength of bond between the surface atom and the adatom, the crystallographic plane of the surface, the accessibility of the surface (e.g., passivation by a capping agent), and the chemical potential gradient.[31a,52] For example, it has been shown that the value of E_{diff} for Rh adatoms diffusing on a closely packed Rh(111) surface was 0.16 eV, while this value increased to 0.60 and 0.88 eV when diffusing on loosely packed Rh(110) and Rh(100) surfaces, respectively.[31a] During an experimental study, adjusting the reaction temperature has become a simple and straightforward approach to the manipulation of $V_{diffusion}$. It should be pointed out that, in many cases, the alteration of parameters such as temperature might also result in changes to both $V_{deposition}$ and $V_{diffusion}$. As a result, one needs to carefully design an experiment to achieve the desired range of values for the ratio of $V_{deposition}$ to $V_{diffusion}$.

4.2. Case Studies. We recently validated the proposed mechanism of kinetic control by studying the growth of Pd cubic seeds whose side faces were passivated by Br^- ions.[53] The experiments were conducted by using a syringe pump to inject an aqueous Na_2PdCl_4 solution (a precursor to elemental Pd) into an aqueous suspension containing L-ascorbic acid (AA, the reductant), PVP (the stabilizer), and 15 nm Pd cubes (the seeds) under magnetic stirring. The reaction solution was hosted in a glass vial immersed in an ice or oil bath held at a

specific temperature. Upon introduction into the reaction solution, the Na_2PdCl_4 precursor should be immediately reduced by AA (a relatively strong reductant) to generate Pd atoms. As a result, the concentration of the newly formed Pd atoms in the reaction solution and therefore the magnitude of $V_{deposition}$ should be proportional to the injection rate of Na_2PdCl_4 solution, which could be tightly controlled with the use of a syringe pump. On the other hand, the magnitude of $V_{diffusion}$ could be adjusted by setting the reaction system to a specific temperature with the use of an ice or oil bath equipped with a temperature controller. Taken together, we could systematically evaluate the roles played by $V_{diffusion}$ and $V_{deposition}$ in controlling the shape of nanocrystals obtained under different experimental conditions.

In the first set of experiments, we singled out and examined the role of $V_{deposition}$ by adjusting the injection rate for Na_2PdCl_4 solution while keeping the reaction temperature fixed at 22 °C. The ratio of $V_{deposition}$ to $V_{diffusion}$ should increase as the injection rate of the Na_2PdCl_4 solution increases because $V_{diffusion}$ is fixed. According to the proposed mechanisms, Pd nanocrystals with all four different shapes shown in Figure 9 should be obtained as the injection rate of the Na_2PdCl_4 solution was increased. As anticipated, Pd cuboctahedrons (Figure 10A), cubes with
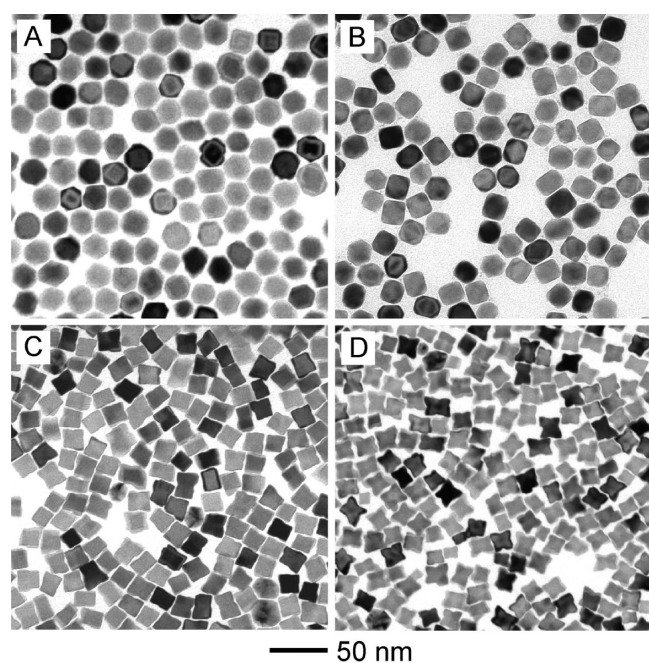

Figure 10. Palladium nanocrystals with four distinctive shapes that were obtained by injecting Na_2PdCl_4 solution into an aqueous suspension containing 15 nm Pd nanocubes, PVP, and ascorbic acid (22 °C) at different injection rates: (A) 0.25, (B) 0.5, (C) 0.75, and (D) 1.5 mL/h. (Reproduced with permission from ref 53. Copyright 2013 National Academy of Sciences.)

slightly truncation at corners (Figure 10B), concave cubes (Figure 10C), and octapods (Figure 10D) were indeed obtained from the same batch of Pd cubic seeds when the injection rate of the Na_2PdCl_4 solution was increased from 0.25 to 0.5, 0.75, and 1.5 mL/h, respectively. To investigate the role played by $V_{diffusion}$, a second set of experiments was conducted by varying the reaction temperature while fixing the injection rate of the Na_2PdCl_4 solution at 0.5 mL/h. In this case, the ratio of $V_{deposition}$ to $V_{diffusion}$ is expected to increase with the

decrease of temperature because $V_{deposition}$ is fixed. According to the pathways outlined in Figure 9, it would not be surprising at all to observe Pd nanocrystals with shapes similar to those shown in Figure 10, A−D, when the reaction temperature was decreased. Indeed, Pd nanocrystals with shapes ranging from cuboctahedrons to cubes with slight truncation at corners, concave cubes, and octapods were all obtained as the products when the reaction temperature was set to 75, 50, 22, and 0 °C, respectively. Collectively, these experimental results not only support our proposed mechanism for kinetic control but also provide synthetic strategies for manipulating the reaction kinetics.

The mechanistic understanding of kinetic control was also successfully extended to many other systems involving the growth of cubic seeds whose side faces were passivated by various capping agents.[19a] Here we just want to highlight an important example related to the synthesis of concave cubes because they are expected to show greatly enhanced properties relative to their convex counterparts owing to the presence of high-index facets as well as sharp corners and edges.[19a,54] In one example, Pd−Pt concave cubes (Figure 11A) were prepared by
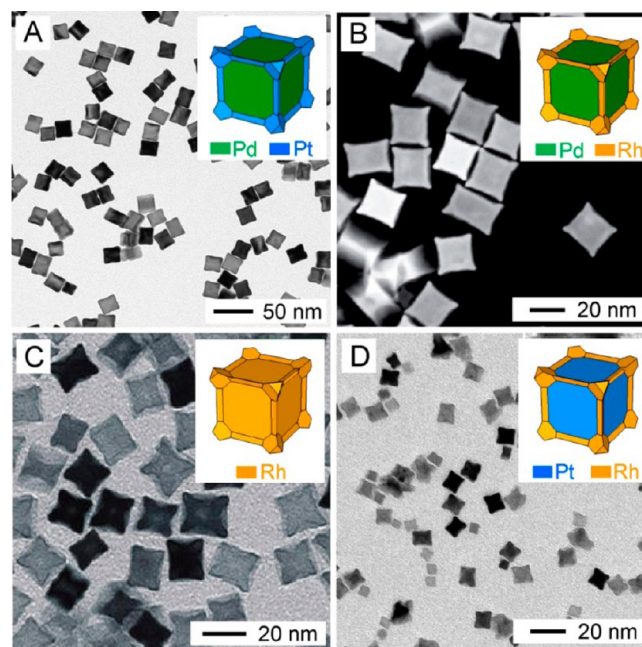

Figure 11. Concave nanocubes comprised of (A) Pd−Pt, (B) Pd−Rh, (C) Rh, and (D) Pt−Rh that were obtained by manipulating the rates of atom deposition and surface diffusion during the seeded growth process. The insets show the corresponding 3-D models of the concave nanocubes. ((A) Adapted with permission from ref 53. Copyright 2013 National Academy of Sciences. (B) Adapted with permission from ref 56. Copyright 2012 Wiley-VCH. (C,D) Adapted with permission from ref 50. Copyright 2011 American Chemical Society.)

injecting a solution of Na_2PtCl_6 (a precursor to elemental Pt) in ethylene glycol at a rate of 8.0 mL/h into an ethylene glycol suspension containing 15 nm Pd cubic seeds, AA, and Br⁻ ions that was held in an oil bath preset to 180 °C.[53] In comparison, the products became Pd−Pt multipods when the reaction temperature was decreased from 180 to 160 °C or lower. Clearly, the key to coating a complete and uniform layer of Pt on Pd cubic seeds was to increase $V_{diffusion}$ and thus decrease the ratio of $V_{deposition}/V_{diffusion}$ by raising the reaction temperature.

This result is again in agreement with the mechanism proposed in Figure 9. It is worth pointing out that the temperature required for the Pt adatom to diffuse from corners to side faces of a Pd cubic seed is significantly higher compared with the case of Pd growth (Figure 10). This difference can be attributed to the following order in terms of bonding energy: E_{Pt-Pt} (307 kJ/mol) > E_{Pt-Pd} (204 kJ/mol) > E_{Pd-Pd} (100 kJ/mol).[55] The relatively larger E_{Pt-Pt} would lead to additional energy barrier to diffusion and thus larger value for E_{diff} in eq 6. The newly formed Pt atoms would prefer to stay at corners to form more stable Pt−Pt bonds rather than to diffuse to side faces and form less stable Pt−Pd bonds.[55b,c] Accordingly, to facilitate the surface diffusion of Pt on Pd, a higher reaction temperature is necessary for overcoming the relatively higher energy barrier to surface diffusion.

Using a similar strategy, Pd−Rh concave nanocubes (Figure 11B) were also prepared by depositing Rh atoms on the surface of Pd cubic seeds at 140 °C.[56] Note that the temperature required for Rh adatoms to diffuse on the surface of Pd cubic seeds is slightly lower than that for Pt adatoms, owing to the fact that the bonding energy for Rh−Rh (285 kJ/mol) is smaller than that for Pt−Pt (307 kJ/mol).[55] Interestingly, the Pd cores in the Pd−Pt and Pd−Rh concave nanocubes could be selectively dissolved using an aqueous etchant containing ferric and bromide ions, generating cubic nanoframes made of Pt and Rh with a highly open structure.[56] These results provide direct evidence to support our argument that the Pt or Rh atoms were exclusively deposited on the corners and edges of a Pd cubic seed when their surface diffusion was limited. In addition to the Pd-based concave cubes, we have also demonstrated a polyol process for the synthesis of Rh concave nanocubes by manipulating the reaction kinetics with a syringe pump to alter the injection rate of Na_3RhCl_6 solution (a precursor to elemental Rh).[50] It was found that Rh concave nanocubes with an average edge length of 15 nm (Figure 11C) could only be obtained when the precursor was injected into the reaction solution at a slow rate of 4.0 mL/h. In comparison, a fast injection rate (e.g., 60 mL/h) resulted in the formation of Rh octapods through the accelerated growth along the ⟨111⟩ directions. It is clear that the slow injection rate for the precursor and thus an appropriate ratio of $V_{deposition}$ to $V_{diffusion}$ were responsible for the formation of Rh concave nanocubes. Notably, these Rh concave nanocubes were produced in the setting of one-pot synthesis. In this regard, the mechanism of kinetic control illustrated in Figure 9 could indeed be adapted to explain the formation of shapes observed in a conventional one-pot synthesis. The same strategy for controlling $V_{deposition}$ and thereby $V_{deposition}/V_{diffusion}$ ratio using a syringe pump could also be applied to generate Pt−Rh concave nanocubes by using Pt cubic seeds with their side faces being capped by Br⁻ ions (Figure 11D).[50]

In addition to the cubic seeds with heavily blocked side faces, the concept of kinetic control can also be extended to cubic seeds with non- or lightly blocked side faces. To this end, we have demonstrated a facile approach to the synthesis of Ag octahedrons with concave side faces by controlling the growth habit of Ag cubic seeds (Figure 12B−E).[57] The synthesis involved the use of Ag nanocubes as seeds in an aqueous system, with AA and $AgNO_3$ serving as a reductant and a salt precursor, respectively. We found that increasing the concentration of AA facilitated the formation of concave octahedrons whereas conventional octahedrons with flat surfaces were produced at a low concentration of AA.
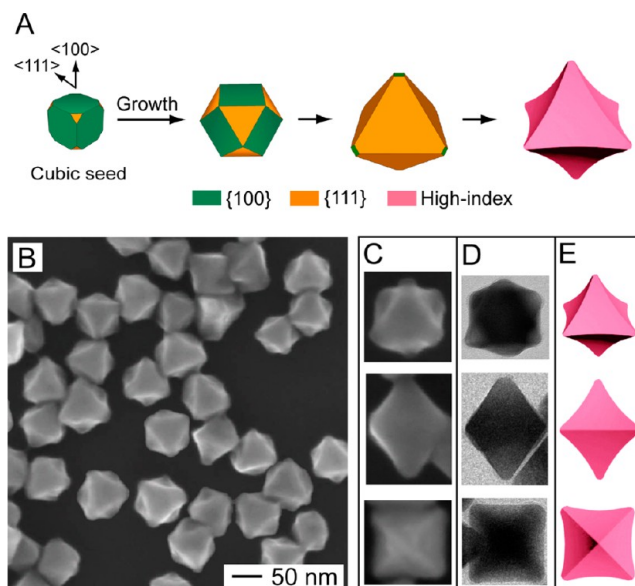
Figure 12. (A) Schematic illustration of the evolution pathway from a Ag cubic seed to a concave octahedron. (B) SEM image of Ag concave octahedrons that were grown from Ag cubic seeds in the presence of ascorbic acid as a reductant at a high concentration. (C) SEM images, (D) TEM images, and (E) models of a concave octahedron orientated along the ⟨111⟩ (top panel), ⟨110⟩ (middle panel), and ⟨100⟩ (bottom panel) directions, respectively. (Adapted with permission from ref 57. Copyright 2011 Wiley-VCH.)

According to the mechanistic insights on kinetic control, we can now easily understand the pathway responsible for the formation of such Ag concave octahedrons. In the absence of adequate PVP in the growth solution as a capping agent for the Ag(100) surface, the side faces of Ag cubic seeds will be able to receive newly formed Ag atoms, leading to growth mainly along the ⟨100⟩ directions (Figure 12A). As a result, cuboctahedrons and octahedrons were formed as intermediates during the growth. Further growth on the octahedrons resulted in the formation of concave octahedrons because the rate of atom deposition at the corners of an octahedron was relatively faster than that of atom diffusion toward the side faces and edges ($V_{deposition} > V_{deposition}$) owing to the use of AA at a high concentration.

To sum up, in order to obtain kinetic products for seed-mediated growth, we need to figure out the sites onto which the atoms newly formed from a salt precursor will be deposited, as well as all possible paths for the adatoms to migrate away through surface diffusion. In principle, the newly formed atoms tend to be added to the site on a growing seed with the highest surface free energy and then migrate to the other sites lower in free energy via surface diffusion. The specific surface free energy (γ) of a seed is determined by the types of facets exposed, the involvement of capping agent, and the presence of twin defects. The specific surface free energy of a facet will decrease when the facet is passivated by a capping agent. The extent of decrease in γ due to the chemisorption of a capping agent is determined by both the type of capping agent and its coverage density on the surface.[58] It should be emphasized that a capping agent can not only lower the γ value of a surface but also increase the energy barrier to surface diffusion.[52] In many cases, the shape taken by the product is a compromise of these two processes. Second, the ratio of $V_{deposition}$ to $V_{diffusion}$ needs to be adjusted to an appropriate range by carefully controlling the

reaction kinetics (see the above discussion in this section for detailed experimental strategies) to achieve the desired shapes.

5. SYMMETRY REDUCTION

Since the lattice of a metal has a highly symmetric structure, there is no intrinsic driving force for it to grow into nanocrystals with geometric symmetry different from its unit cell. For a single-crystal seed made of an fcc metal, its tends to grow into a highly symmetric shape such as cube, cuboctahedron, or octahedron depending on the relative growth rates along the ⟨100⟩ and ⟨111⟩ directions.[59] When prepared using a highly isotropic medium, nanocrystals with reduced symmetry can only be obtained by breaking the intrinsic confinement imposed by the cubic symmetry of its unit cell during the course of growth. In general, the symmetry can be reduced through three major mechanisms: (i) incorporation of twin defects or stacking faults into the crystal lattice in the nucleation step; (ii) induction of an asymmetric deposition pattern for a symmetric seed in the growth step; and (iii) aggregation or attachment of seeds during growth. The first approach can naturally break the symmetry of an fcc lattice through the inclusion of twin defects. Notable examples include the formation of decahedral, icosahedral, and plate-like seeds, followed by their growth into five-fold twinned nanorods or nanowires with a pentagonal cross-section or nanoplates with a triangular or hexagonal profile.[60] Despite these and other demonstrations, the mechanism responsible for the appearance of twin defects or stacking faults during self-nucleation is still unknown, making it impossible to intentionally incorporate them into a seed.[49b]

Here we specifically focus on the second approach based on the induction of asymmetric growth patterns on single-crystal seeds made of an fcc metal. Although several examples of asymmetric growth have been previously reported, including the evolution from single-crystal, cuboctahedral seeds into Au nanorods,[61] Ag or Pd nanobars/nanorods,[46a,62] and anisotropi-cally truncated Ag octahedrons,[63] most of these syntheses lack a mechanistic understanding and/or experimental control. With the insights we have learnt from recent studies, we realized that the products obtained from asymmetric growth typically display anisotropic, thermodynamically less favorable shapes. For example, in an ideal situation, the concentric core−shell nanocubes (Figure 13A, top trace), resulting from the deposition of atoms of a second metal onto all six side faces of a cubic seed, are thermodynamically more favorable than both the non-concentric nanocubes (Figure 13A, middle trace) and hybrid dimers (Figure 13A, bottom trace) originated from the selective growth along three adjacent and one of the six side faces of a cubic seed, respectively. In a sense, the asymmetric growth of highly symmetric seeds can only be induced through kinetic control. Inspired by this mechanistic understanding, we have demonstrated an effective method for reducing the geometric symmetry of a metal nanocrystal by simply manipulating the rate at which metal atoms were generated and deposited from a precursor. As shown in Figure 13B, the growth pattern will automatically become asymmetric when the number of atoms available is smaller than the number of equivalent sites on the surface of a seed. This is particularly important in the very early stage of a seeded growth process because the growth pattern will be essentially retained once it has been initiated when surface diffusion is relatively slow.

In an initial study, we examined the growth of Ag on Pd cubic seeds in an aqueous system at room temperature.[64] The
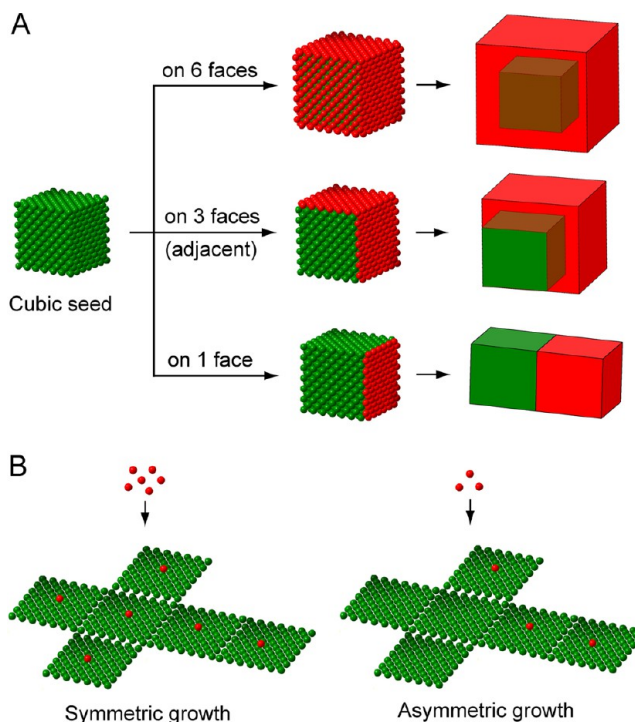
Figure 13. (A) Schematic illustration of three possible pathways for the nucleation and growth of a cubic seed. (B) Schematic illustrations of two different growth patterns on the six side faces of a cubic seed, as determined by the number of newly formed atoms relative to the number of seeds in the growth solution.

typical synthesis involves the use of 18 nm Pd nanocubes as seeds, together with AA, $AgNO_3$, and PVP serving as the reductant, precursor to Ag, and stabilizer, respectively. As shown in Figure 14, the growth could be directed to selectively take place on six, three, or one of the faces of a cubic seed by simply decreasing the injection rate of the $AgNO_3$ solution, resulting in the formation of Pd−Ag concentric core−shell nanocubes, Pd−Ag non-concentric core−shell nanocubes, and Pd−Ag hybrid dimers, respectively. The initial deposition patterns of the newly formed Ag atoms on the surface of a Pd seed is mainly responsible for the asymmetric growth pathways and thus the formation of different types of Pd−Ag bimetallic nanocrystals. In this synthesis, the initial concentration of Ag atoms in the reaction solution was mainly determined by the injection rate of $AgNO_3$ that could be tightly controlled through the use of a syringe pump. At a fast injection rate, a large number of Ag atoms will collide with the surface of each Pd seed and thereby the activation of all sites for growth. In this case, each side face of a Pd seed will have a chance to receive the newly formed Ag atoms, and Pd−Ag concentric core−shell nanocubes will be formed (Figure 14A−D). When the injection rate is extremely slow, the concentration of Ag atoms around a cubic seed will become too low to ensure collision and nucleation on all the six faces of a cubic seed. Instead, only one of the six side faces of a cubic seed will be able to receive the newly formed Ag atoms, leading to the formation of Pd−Ag hybrid dimers (Figure 14I−L). A similar mechanism is also involved when $AgNO_3$ is injected at a moderate rate. In this case, the small number of Ag atoms generated from the precursor will only be enough to cover three of the six faces of a cubic seed, and a Pd−Ag non-concentric nanocubes will be obtained (Figure 14E−H). The reason why Ag preferred to
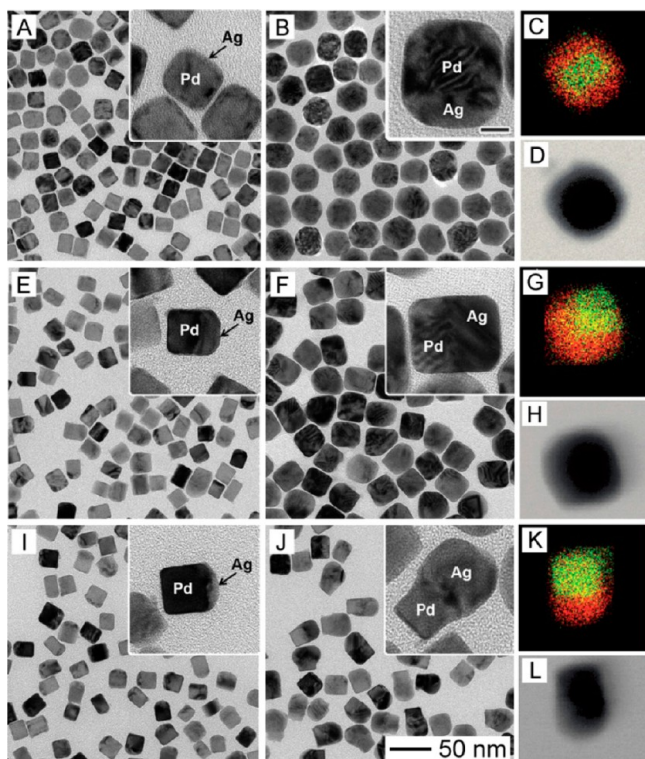
Figure 14. Synthesis of different types of Pd–Ag bimetallic nanocrystals by controlling the injection rate of AgNO$_3$ (precursor to Ag) solution during the growth of Pd cubic seeds. (A,B) TEM images of Pd–Ag concentric core–shell nanocubes obtained by adding all the precursor solution in one shot with a pipet; the total volumes of precursor added were (A) 0.5 and (B) 3.3 mL. (C) EDX mapping and (D) bright-field STEM image of a single Pd–Ag concentric core–shell nanocube shown in (B). (E,F) Pd–Ag non-concentric nanocubes obtained by injecting the precursor solution at 30 mL/h; the total volumes of precursor added were (E) 0.5 and (F) 3.3 mL. (G) EDX mapping and (H) bright-field STEM image of an individual Pd–Ag non-concentric nanocube shown in (F). (I,J) Pd–Ag hybrid dimers obtained by injecting the precursor solution at 1 mL/h; the total volumes of precursor added were (I) 0.4 and (J) 2.7 mL. (K) EDX mapping and (L) bright-field STEM image of an individual Pd–Ag hybrid dimer shown in (J). The insets in the TEM images show individual nanocyrstals at a higher magnification. The scale bar in the inset of (B) is 10 nm and applies to all other insets. (Reproduced with permission from ref 64. Copyright 2011 Wiley-VCH.)

deposit on three adjacent faces instead of other combinations might be related to the collision pattern of Ag atoms with the seed, as well as the surface diffusion of Ag adatoms. It should be pointed out that, once a cluster (or nucleus) of Ag atoms has been created on a certain face of the seed, the deposition of atoms in the following step will preferentially occur at this site rather than other sites due to the involvement of a lower energy barrier. The site-specific growth can be retained as long as the atom deposition rate is faster than the surface diffusion rate of adatoms.

In a follow-up study, we further demonstrated that Ag could be selectively deposited to initiate growth on any number of faces of a Pd cubic seed by carefully controlling a set of experimental parameters (e.g., the injection rate of Ag precursor, pH value, type of reducing agent, and reaction temperature) that determine the reaction kinetics.[65] In addition, this approach was successfully extended to the Pd–Au system to obtain bimetallic nanostructures with morphol-

ogies similar to what is shown in Figure 14. These results provided sufficient evidence to support our argument that asymmetric growth is induced and maintained by kinetic control. It is worth mentioning that the deposition of Ag or Au atom on a Pd cubic seed was found to selectively take place on the Br$^-$ ions-blocked side faces rather than corners, which is different from the deposition of Pd, Pt, and Rh atoms of Pd cubic seeds. Such preferential deposition on side faces might be ascribed to the formation of insoluble AgBr ($K_{sp} = 5.5 \times 10^{-13}$) or AuBr$_3$ ($K_{sp} = 4.0 \times 10^{-36}$) that can serve as nucleation sites.[66]

For the above cases, Ag or Au adatoms on one of the faces of a Pd cubic seed may have the possibility to diffuse to adjacent faces, but it should be much more difficult than the "vertex-to-face" or "edge-to-face" diffusion paths owing to involvement of relatively large energy barriers for the latter two cases. In addition, all the syntheses were conducted at room temperature (i.e., around 22 °C). This relatively low temperature further depresses the rate of surface diffusion. Therefore, the impact of surface diffusion can be ignored and the localized, asymmetric growth pattern could be well-retained during the entire course of growth. However, in some cases, the effect of surface diffusion will be more significant and has to be taken into account. For example, we found that surface diffusion had a great impact on the asymmetric growth of Cu on a Pd cubic seed.[67] The growth of Cu involved the reduction of CuCl$_2$ by glucose at 100 °C in the presence of 18 nm Pd cubes as seeds and hexadecylamine as a capping agent for Cu{100} facet. In the initial stage (Figure 15A), Cu atoms only nucleated and grew on one or two of the side faces of a Pd cubic seed. Later on, Cu adatoms on one side face started to migrate to other faces through surface diffusion, resulting in an incomplete
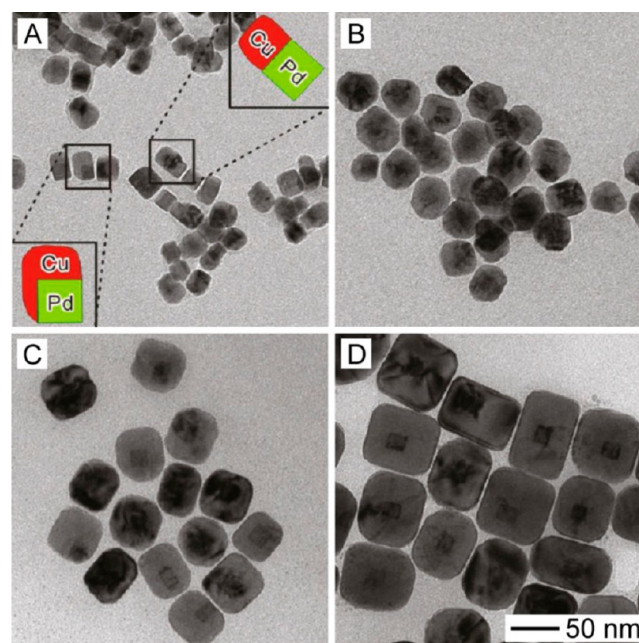
Figure 15. Growth of Cu on 18 nm Pd cubic seeds in the presence of glucose as a reductant and hexadecylamine as a capping agent for the Cu(100) surface at 100 °C. (A–D) TEM images of products sampled at different stages of a synthesis involving the deposition of Cu on Pd cubic seeds: (A) 20, (B) 40, (C) 60, and (D) 180 min. The scale bar in (D) applies to (A–C). (Reproduced with permission from ref 67. Copyright 2012 American Chemical Society.)

coating of Cu shells on Pd seed (Figure 15B). As surface diffusion continued, the entire surface of a Pd seed was eventually encased by a Cu shell to generate a Pd–Cu core–shell nanocrystal (Figure 15C,D). The core–shell nanocrystals took a cubic shape with {100} facets expressed on the surface because of the selective capping of Cu{100} facets by hexadecylamine. We believe the low rate of atom supply caused by the use of a much weaker reductant (i.e., glucose) relative to AA is responsible for the asymmetric growth mode. On the other hand, the observed diffusion of Cu adatoms from one side face of a Pd cubic seed to another during the growth could be ascribed to the relatively high reaction temperature (i.e., 100 °C). Owing to the initial asymmetric growth mode, the Pd seeds tended not to be positioned in the centers of the Pd–Cu nanocubes (Figure 13D). Compared with the Pd–Cu hybrid dimers formed in the initial stage, the symmetry of the final non-concentric Pd–Cu nanocubes was somewhat increased. In a sense, the involvement of surface diffusion can possibly offset the process of symmetry reduction during asymmetric growth.

The symmetry reduction based on kinetic control can also be extended to other systems such as the growth of Ag on Ag cubic seeds.[68] The growth condition was similar to what was used for the Pd–Ag system shown in Figure 14, except for the use of Ag cubes as the seeds and the involvement of PVP in different concentrations. Like the Pd–Ag system, the growth of a Ag cubic seed could be directed to selectively take place on six, three, or one of the faces depending on the injection rate for the AgNO$_3$ solution. Like the case of symmetric growth shown in Figure 7, the facets expressed on the resultant Ag nanocrystals and their proportions were determined by the concentration of PVP in the reaction solution. At a relatively low concentration of PVP (1.0 mg/mL), {111} facets were developed immediately after the growth had been initiated due to the inadequate passivation by PVP (Figure 16, panels B, E, and H) and these facets were gradually enlarged in area at the expense of {100} facets (Figure 16, panels C, F, and I). Eventually, Ag octahedrons (Figure 16D), 3/6-truncated octahedrons (Figure 16G), and 5/6-truncated octahedrons (Figure 16J) were obtained as the final products at fast, moderate, and slow injection rates, respectively, for the AgNO$_3$ solution. In the presence of PVP at a relatively high concentration of 30 mg/mL, the initially formed Ag nanocrystals showed only {100} facets on the surface. Accordingly, the Ag cubic seeds grown into cubes, cubes, and bars with an average aspect ratio of 1.2, respectively, at fast, moderate, and slow injection rates for the AgNO$_3$ solution. As the growth proceeded, the cubes and bars started to show truncations at the corners due to the depletion of PVP from the reaction solutions, and they eventually evolved into octahedrons, 3/6-truncated octahedrons, and elongated 5/6-truncated octahedrons, respectively. To understand the difference in exposed facets for the resultant Ag nanocrystals, we have to take into account the factor of thermodynamic control too. In the absence or the presence of PVP at a relatively low concentration, the surface free energy of Ag{111} was lower than that of Ag{100}. As soon as a cubic seed is initiated for growth, the {100} facets will be gradually replaced with the more stable {111} facets, which is consistent with the results shown in Figure 7. In the presence of PVP at a high concentration, however, the order of $\gamma_{\{100\}}$ and $\gamma_{\{111\}}$ would be reversed. In the initial stage of growth, the nanocrystals tended to expose the more stable {100} faces as a result of PVP
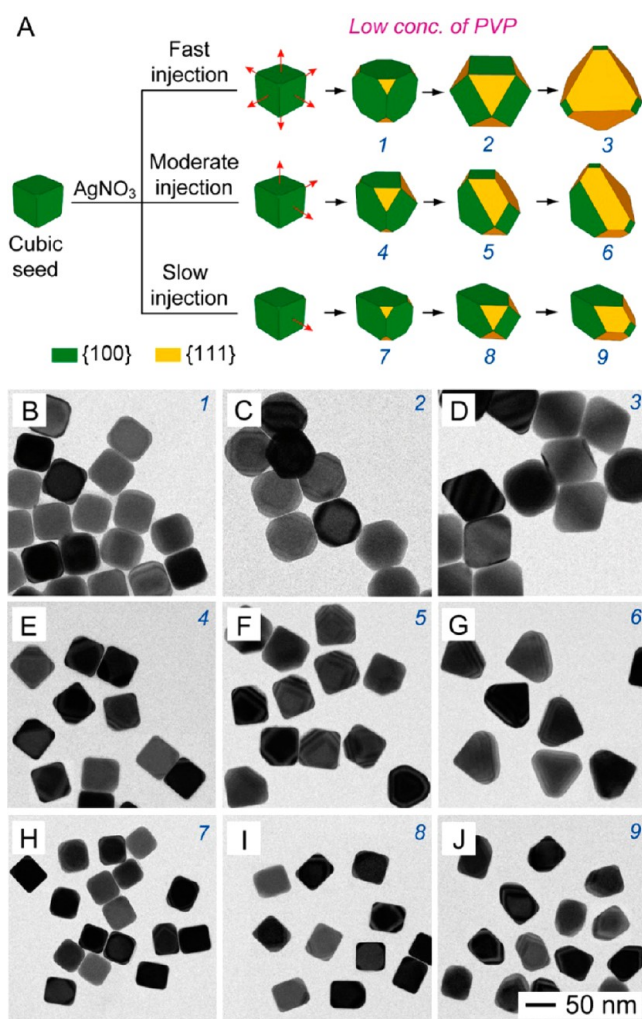
Figure 16. Growth pathways for Ag cubic seeds in an aqueous system in the presence of PVP at a relatively low concentration of 1.0 mg/mL. (A) Morphological changes for the Ag nanocrystals formed at three different injection rates for the AgNO$_3$ solution. (B–J) TEM images showing the evolution of shapes for Ag nanocrystals with the growth occurring on (B–D) six, (E–G) three, and (H–J) one of the six faces of a cubic seed. The volume of AgNO$_3$ injected was (B) 1.2, (C) 2.5, and (D) 3.5 mL at a rate of 100 mL/h; (E) 0.5, (F) 1.1, and (G) 1.6 mL at a rate of 8.0 mL/h; and (H) 0.2, (I) 0.4, and (J) 0.7 mL at a rate of 0.7 mL/h, respectively. The number under each 3-D model matches the number on the TEM image. The 50 nm scale bar in (J) applies to (B–I). (Adapted with permission from ref 68. Copyright 2012 American Chemical Society.)

capping. However, as PVP was gradually consumed and thus depleted from the solution, the newly formed {100} facets could no longer be passivated by PVP and {111} facets would start to appear. These results indicate that the asymmetric growth pattern is induced by kinetic control while the facets exposed on the final products are mainly determined by thermodynamic control. In a sense, a combination of both thermodynamic and kinetic controls can give rise to a wider variety of nanocrystals with asymmetric shapes.

More recently, we demonstrated that, in addition to the use of a syringe pump and a weak reductant, kinetically induced asymmetric growth could also be accomplished by altering the type of a salt precursor.[69] Specifically, Pd cuboctahedral seeds could be directed to evolve into octahedrons with increasing sizes via a symmetric growth pattern (Figure 17A, upper trace)
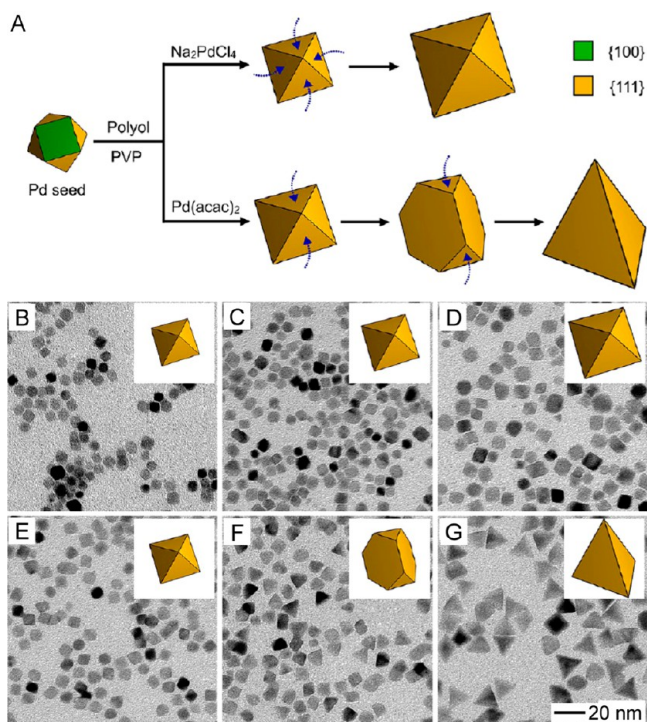
Figure 17. (A) Formation of Pd octahedrons and tetrahedrons when Na_2PdCl_4 and $Pd(acac)_2$, respectively, were used as precursors for the growth of Pd cuboctahedral seeds in a polyol system. The blue arrows denote the deposition of Pd atoms resulting from the reduction of precursor. (B–G) TEM images showing the shape evolution of cuboctahedral seeds at different growth stages when (B–D) Na_2PdCl_4 and (E–G) $Pd(acac)_2$ were employed as precursors, respectively. The samples were collected at different time points in the synthesis: (B,E) 0.5, (C,F) 1.5, and (D,G) 10 min. The insets in (B–G) show 3-D models of the corresponding products obtained at different time points. The 20 nm scale bar in (G) applies to (B–F). (Reproduced with permission from ref 69. Copyright 2013 American Chemical Society.)

or octahedrons, truncated tetrahedrons, and then tetrahedrons via an asymmetric growth pattern (Figure 17A, lower trace) when Na_2PdCl_4 or $Pd(acac)_2$ was used as the precursor in a polyol synthesis. The observed difference in growth pattern was attributed to the different reduction rates of these two precursors. The newly formed Pd atoms resulting from the reduction of Pd precursor tended to be deposited on the {100} facets (in this case, free of Br^- ions) of a Pd cuboctahedral seed due to the higher surface free energy of {100} relative to that of {111}. As such, the cuboctahedral seeds would grow into octahedrons in the initial stage for both cases involving the use of Na_2PdCl_4 and $Pd(acac)_2$ as precursors. Notably, the edge length of the octahedrons obtained in the early stage of a synthesis involving $Pd(acac)_2$ was relatively larger than the octahedrons obtained with Na_2PdCl_4 as the precursor (7.1 nm vs 5.5 nm at $t = 0.5$ min, as shown in Figure 17B,E). This difference suggests that more Pd^{2+} ions had been reduced to Pd(0) atoms and subsequently included into the Pd octahedrons for the case of $Pd(acac)_2$ owing to its faster reduction rate, which was also validated by the ICP-MS data for the measurements of remaining Pd^{2+} in a reaction solution. As such, in the later stage, the newly formed Pd atoms through the reduction of $Pd(acac)_2$ would be inadequate to nucleate on all of the eight {111} facets of a Pd octahedron. Instead, only four of the eight {111} facets of an octahedron could be involved in

the heterogeneous nucleation and growth, leading to the transformation from octahedrons to truncated tetrahedron (Figure 17F) and finally tetrahedron (Figure 17G). In contrast, when Na_2PdCl_4 was used as a precursor, the relatively high concentration of Pd^{2+} remaining in the reaction solution in the early stage of a synthesis allowed the nucleation to occur on all eight facets of the preformed Pd octahedrons. As a result, all of the eight {111} facets underwent growth, resulting in the formation of Pd octahedrons with gradually increasing sizes (Figure 17C,D). These results again demonstrated that the asymmetric growth of a highly symmetric seed can only be achieved under kinetic control.

6. CONCLUSIONS AND OUTLOOK

Through this Perspective, we have communicated our current mechanistic understanding on the role played by a thermodynamic or kinetic parameter in dictating the shape evolution of colloidal metal nanocrystals, as exemplified by the growth of single-crystal seeds encased by a mix of {100}, {111}, and {110} facets. The essence of thermodynamic control is to minimize the total surface free energy of a system. Without the involvement of surface capping (like the case in a vacuum), metal nanocrystals should take the Wulff shape (i.e., truncated octahedron or cuboctahedron for an fcc metal). In the presence of a capping agent, however, the final product is no longer constrained by the Wulff shape derived for the case of vacuum. The types of facets exposed on the surface and their proportions can both be controlled by intentionally introducing a capping agent into a synthesis at a proper concentration. In order to achieve the shape determined by thermodynamics, the atoms deposited on the surface of a seed during a growth process should be able to diffuse to the lowest-energy sites. In reality, however, when the rate of surface diffusion is slower than that for atom deposition, the shape can be trapped in a thermodynamically unstable, but kinetically enabled, state. Any activity involving the manipulation of rate for either surface diffusion or atom deposition should be considered as kinetic control, which can be most conveniently achieved by reducing the temperature used for a synthesis. It can also be accomplished by other means, including variations to the types of reductant and precursor, concentrations of reagents, pH value, as well as the introduction of additives. As the hallmark of a kinetically controlled process, the products are no longer constrained by the thermodynamic confinement, allowing for the formation of nanocrystals with high-index facets, concave surfaces, and branched arms. Significantly, kinetic control can also force a highly symmetric seed to undergo asymmetric growth, producing nanocrystals with reduced symmetry. In this case, the supply of newly formed atoms must be kept at a sufficiently low level so that they could only nucleate and then grow on a limited number of equivalent sites on the surface of a seed. Of course, one has to decelerate surface diffusion by reducing the reaction temperature in order to retain the asymmetric growth pattern.[70] Over the past two decades, colloidal metal nanocrystals with a myriad of different shapes have been successfully prepared by developing protocols based on the concepts of both thermodynamic and kinetic control.

Despite the incredible progress in understanding and experimentally controlling the evolution from seeds to nanocrystals with diversified shapes, the field of colloidal nanocrystal synthesis still faces a number of challenges. Here

we would like to offer a short list of directions or themes for the future research in this field:

(a) Gaining insights into the nucleation process. Most of the mechanistic understandings with respect to thermodynamic or kinetic control discussed in this article are based on studies of the evolution from seeds to nanocrystals in the setting of seeded growth. There is very little knowledge of the exact mechanism responsible for the nucleation step in a one-pot synthesis. As such, it remains a daunting challenge to elucidate the explicit roles played by various thermodynamic and kinetic factors in a one-pot synthesis.[49b] This challenge is mainly imposed by the shortage of instruments capable of capturing, identifying, and monitoring the evolution from atoms to nuclei and then seeds with satisfying resolution. In this regard, alternative approaches based on computational simulations may help us decipher the secret in the black box of nucleation.

(b) Enhancing the quality and increasing the diversity of seeds. As demonstrated by many examples throughout this article, well-defined seeds are essential to the investigation of shape evolution governed by thermodynamic and kinetic control. Seeds with high purity and narrow size distribution not only make it easier to monitor the overall shape evolution during growth but also ensure high quality for the final products. At the current stage of development, the lack of a mechanistic understanding of the nucleation process makes it very challenging to generate high-quality seeds for all metals. In most cases, the seeds are comprised of a mixture of nanocrystals with broad distributions in terms of size, shape, and twin structure. Purification is a potentially useful approach to the refinement of seeds, and techniques including density gradient centrifugation, membrane-based filtration, solvent extraction, and electrophoresis can all be employed to effectively separate and purify seeds with different sizes and shapes. To enhance the quality and increase the diversity of seeds, one can also carefully control the reaction conditions. Most recently, we demonstrated the feasibility to quantitatively correlate the type of seeds formed with the initial reduction rate involved in a synthesis (Figure 18).[49b] With Pd as an example, we demonstrated that kinetic parameters, including rate constant and activation energy, could be derived from spectroscopic measurements and used to calculate the initial reduction rate and then have this parameter quantitatively correlated with the twin structure of a seed. On a quantitative basis, we were able to determine the ranges of initial reduction rates required for the formation of seeds with a single-crystal, multiply twinned, or stacking fault-lined structure. This new development represents a major step forward toward the deterministic syntheses of colloidal metal nanocrystals with specific twin structures and geometric shapes.

(c) Better understanding the processes of atom deposition and surface diffusion. In Section 5, we have demonstrated the importance of atom deposition rate and surface diffusion rate in governing the evolution of a seed into nanocrystals with diversified shapes. However, it is still unclear how atoms are actually deposited onto the surface of a seed and how they migrate to different sites
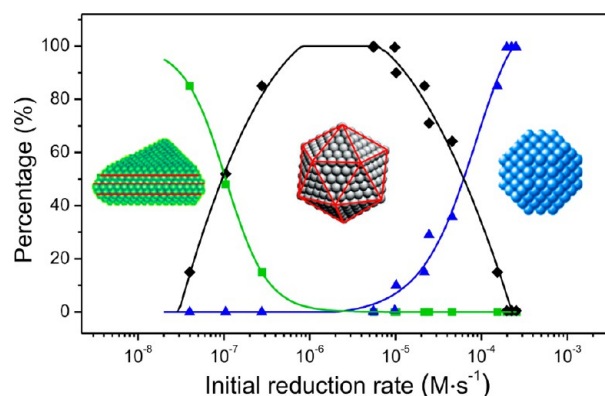
Figure 18. Plot showing the percentages of Pd nanocrystals with different twin structures as a function of the initial reduction rate of a synthesis. The relative distribution of single-crystal, multiply twinned, and stacking fault-lined structures were acquired using TEM imaging and are denoted in blue, black, and green, respectively. The twinned planes or stacking faults are delineated in red. (Reproduced with permission from ref 49b. Copyright 2015 American Chemical Society.)

on the surface. Owing to the involvement of a solution phase and the Brownian motion of a growing seed, it is extremely difficult to directly follow the deposition of atoms on a seed and their subsequent diffusion in real space despite the remarkable advancement in *in situ* electron microscopy.[71] Again, alternative approaches based on computational simulations may greatly advance our understanding of this subject.

(d) Systematic screening and evaluation of the capping agents. Although a rich variety of capping agents have been identified for controlling the shapes of metal nanocrystals, it is still obscure about how these capping agents work in terms of binding selectivity toward a specific metal surface. There is essentially no experimental tool capable of resolving the configuration and packing of capping agents on the surface of a nanocrystal. In addition, it remains a grand challenge to quantitatively analyze the binding affinity and coverage density of a capping agent toward the surface of a metal nanocrystal. We have to largely rely on the use of computational modeling to advance our understanding of the role of a surface capping agent. Screening new capping agents that can selectively passivate the different types of facets of a specific metal is an interesting and important issue that deserves thorough exploration in the near future.

(e) Precise control of the reaction kinetics. In general, the reaction kinetics involved in a nanocrystal synthesis can be manipulated by controlling all experimental conditions related to reaction kinetics. In most cases, however, changing one reaction parameter will inevitably bring in unexpected complications, making it difficult to precisely control the reaction kinetics. For example, the introduction of an oxidative etchant such as Cl^-/O_2,[72] $Fe(II)/Fe(III)$,[73] and $Cu(I)/Cu(II)$[74] has proven to be an effective strategy for kinetically controlling the morphology of noble-metal nanocrystals by retarding the rate of atom supply from a precursor. Besides the effect on reaction rate, however, the introduction of such ionic species may cause changes to the pH value and formation of unexpected coordination compounds that will alter the reaction kinetics. Therefore, one needs to

carefully consider all the possible variations to reaction kinetics when changing an experimental parameter.

(f) Deeper understanding of asymmetric growth. As showcased in section 5, asymmetric growth is a powerful approach to greatly expanding the shape diversity of nanocrystals. Yet, asymmetric growth is much complicated in comparison with symmetric growth. We have demonstrated that kinetic control is an effective way to induce and direct the growth of a highly symmetric seed into asymmetric patterns and thus produce various anisotropic mono- and bimetallic nanocrystals. However, a quantitative understanding of the correlation between growth pattern and reduction kinetics is still lacking. To this end, quantitative measurements of experimental parameters related to asymmetric growth, such as the deposition rate of atoms, the total surface area of seeds, and possibility of collision between atoms and seeds, are all very useful information that deserves further investigation. With these quantitative data, the strategy of kinetic control can be readily extended to other systems that may involve different types of seeds and metals.

Ultimately, we hope that the mechanistic understandings and experimental strategies provided in this Perspective can serve as a resource or starting point for people who want to develop colloidal metal nanocrystals with desired shapes and properties for applications in areas as diverse as catalysis, plasmonics, sensing/imaging, spectroscopy, and medicine. As the "mother nature" of this kind of work, the mechanistic understandings will be constantly refined and developed as our experimental capabilities and computational insights are advanced.

■ AUTHOR INFORMATION

Corresponding Author
*younan.xia@bme.gatech.edu
Author Contributions
§X.X. and H.-C.P. contributed equally to the preparation of this Perspective.
Notes
The authors declare no competing financial interest.

■ ACKNOWLEDGMENTS

■ REFERENCES

(1) (a) Lewis, L. N. Chem. Rev. **1993**, 93, 2693−2730. (b) Somorjai, G. A. Chem. Rev. **1996**, 96, 1223−1236. (c) Aiken, J. D., III; Finke, R. G. J. Mol. Catal. A-Chem. **1999**, 145, 1−44. (d) Ertl, G. Handbook of Heterogeneous Catalysis; Wiley-VCH, Weinheim, 2008. (e) Leenders, S.; Gramage-Doria, R.; Bruin, B.; Reek, J. Chem. Soc. Rev. **2015**, 44, 433−448.

(2) (a) Lay, G. L. Sur. Sci. **1983**, 132, 169−204. (b) Davey, N. M.; Seymour, R. J. Platinum Met. Rev. **1985**, 29, 2. (c) Okinaka, Y.; Hoshino, M. Gold Bull. **1998**, 31, 3−13. (d) Jeong, S.; Woo, K.; Kim, D.; Lim, S.; Kim, J. S.; Shin, H.; Xia, Y.; Moon, J. Adv. Funct. Mater. **2008**, 18, 679−686. (e) Talapin, D. V.; Lee, J.-S.; Kovalenko, M. V.; Shevchenko, E. V. Chem. Rev. **2010**, 110, 389−458.

(3) (a) Maier, S. A.; Brongersma, M. L.; Kik, P. G.; Meltzer, S.; Requicha, A. A. G.; Atwater, H. A. Adv. Mater. **2001**, 13, 1501−1505. (b) Kauranen, M.; Zayats, A. V. Nat. Photonics **2012**, 6, 737−748. (c) Gupta, M. C.; Ballato, J. The Handbook of Photonics; CRC Press, Taylor & Francis Group: Boca Raton, 2006. (d) Koenderink, A. F.; Alù, A.; Polman, A. Science **2015**, 348, 516−521.

(4) (a) Murray, C. B.; Sun, S.; Doyle, H.; Betley, T. MRS Bull. **2001**, 26, 985−991. (b) Kozicki, M. N.; Mitkova, M.; Park, M.; Balakrishnan, M.; Gopalan, C. Superlattices Microstruct. **2004**, 34, 459−465. (c) Ditlbacher, H.; Lamprecht, B.; Leitner, A.; Aussenegg, F. R. Opt. Lett. **2000**, 25, 563−565.

(5) (a) Nozik, A. J.; Miller, J. Chem. Rev. **2010**, 110, 6443−6445. (b) Linic, S.; Christopher, P.; Ingram, D. B. Nat. Mater. **2011**, 10, 911−921. (c) Jena, P. J. Phys. Chem. Lett. **2011**, 2, 206−211.

(6) (a) Cohn, J. G. Environ. Health Perspect. **1975**, 10, 159−164. (b) Colvin, V. L. Nat. Biotechnol. **2003**, 21, 1166−1170. (c) Parks, J. E., II. Science **2010**, 327, 1584−1585.

(7) (a) West, J. L.; Halas, N. J. Annu. Rev. Biomed. Eng. **2003**, 5, 285−292. (b) Alivisatos, P. Nat. Biotechnol. **2004**, 22, 47−52. (c) Jain, P. K.; El-Sayed, I. H.; El-Sayed, M. A. Nano Today **2007**, 2, 18−29. (d) Burda, C.; Chen, X.; Narayanan, R.; El-Sayed, M. A. Chem. Rev. **2005**, 105, 1025−1102. (e) Xia, Y.; Li, W.; Cobley, C. M.; Chen, J.; Xia, X.; Zhang, Q.; Yang, M.; Cho, E. C.; Brown, P. K. Acc. Chem. Res. **2011**, 44, 914−924. (f) Howes, P. D.; Chandrawati, R.; Stevens, M. M. Science **2014**, 346, 1247390.

(8) (a) Grzelczak, M.; Pérez-Juste, J.; Mulvaney, P.; Liz-Márzan, L. M. Chem. Soc. Rev. **2008**, 37, 1783−1791. (b) Camden, J. P.; Dieringer, J. A.; Zhao, J.; Van Duyne, R. P. Acc. Chem. Res. **2008**, 41, 1653−1661. (c) Burda, C.; Chen, X.; Narayanan, R.; El-Sayed, M. A. Chem. Rev. **2005**, 105, 1025−1102.

(9) (a) Rycenga, M.; Cobley, C. M.; Zeng, J.; Li, W.; Moran, C. H.; Zhang, Q.; Qin, D.; Xia, Y. Chem. Rev. **2011**, 111, 3669−3712. (b) Eustis, S.; El-Sayed, M. A. Chem. Soc. Rev. **2006**, 35, 209−217. (c) Mayer, K. M.; Hafner, J. H. Chem. Rev. **2011**, 111, 3828−3857. (d) Willets, K. A.; Van Duyne, R. P. Annu. Rev. Phys. Chem. **2007**, 58, 267−297. (e) Xia, Y.; Halas, N. J. MRS Bull. **2005**, 30, 338−348.

(10) (a) Faraday, M. Philos. Trans. R. Soc. London **1857**, 147, 145−181. (b) Mulvaney, P. Langmuir **1996**, 12, 788−800.

(11) (a) Murphy, C. J.; Sau, T. K.; Gole, A. M.; Orendorff, C. J.; Gao, J.; Gou, L.; Hunyadi, S. E.; Li, T. J. Phys. Chem. B **2005**, 109, 13857−13870. (b) Lee, K. S.; El-Sayed, M. A. J. Phys. Chem. B **2005**, 109, 20331−20338. (c) Ye, X.; Jin, L.; Caglayan, H.; Chen, J.; Xing, G.; Zheng, C.; Doan-Nguyen, V.; Kang, Y.; Engheta, N.; Kagan, C. R.; Murray, C. B. ACS Nano **2012**, 6, 2804−2817. (d) Brioude, A.; Jiang, X. C.; Pileni, M. P. J. Phys. Chem. B **2005**, 109, 13138−13142.

(12) (a) McLellan, J. M.; Li, Z.-Y.; Siekkinen, A. R.; Xia, Y. Nano Lett. **2007**, 7, 1013−1017. (b) Mulvihill, M.; Tao, A.; Benjauthrit, k.; Arnold, J.; Yang, P. Angew. Chem., Int. Ed. **2008**, 47, 6456−6460. (c) Aslan, K.; Lakowicz, J. R.; Geddes, C. D. Anal. Bioanal. Chem. **2005**, 382, 926−933. (d) Ming, T.; Zhao, L.; Yang, Z.; Chen, H.; Sun, L.; Wang, J.; Yan, C. Nano Lett. **2009**, 9, 3896−3903.

(13) (a) Narayanan, R.; El-Sayed, M. A. Nano Lett. **2004**, 4, 1343−1348. (b) Guo, S.; Zhang, S.; Sun, S. Angew. Chem., Int. Ed. **2013**, 52, 8526−8544. (c) Xie, S.; Choi, S.-I.; Xia, X.; Xia, Y. Curr. Opin. Chem. Eng. **2013**, 2, 142−150.

(14) Bratlie, K. M.; Kilewer, C. J.; Somorjai, G. A. J. Phys. Chem. B **2006**, 110, 17925−17930.

(15) Shao, M.; Yu, T.; Odell, J. H.; Jin, M.; Xia, Y. Chem. Commun. **2011**, 47, 6566−6568.

(16) Stamenkovic, V. R.; Fowler, B.; Mun, B. S.; Wang, G.; Ross, P. N.; Lucas, G. A.; Marković, N. M. Science **2007**, 315, 493−497.

(17) See, for example: (a) Mostafa, S.; Behafarid, F.; Croy, J. R.; Ono, L. K.; Li, L.; Yang, J. C.; Frenkel, A. I.; Cuenya, B. R. J. Am. Chem. Soc. **2010**, 132, 15714−15719. (b) Xu, R.; Wang, D.; Zhang, J.; Li, Y. Chem.—Asian J. **2006**, 1, 888−893. (c) Lee, I.; Morales, R.; Albiter, M. A.; Zaera, F. Proc. Natl. Acad. Sci. U.S.A. **2008**, 105, 15241−15246.

(d) Tian, N.; Zhou, Z. Y.; Sun, S. G.; Ding, Y.; Wang, Z. L. *Science* **2007**, *316*, 732−735.

(18) (a) Xia, Y.; Xiong, Y.; Lim, B.; Skrabalak, S. E. *Angew. Chem., Int. Ed.* **2009**, *48*, 60−103. (b) Tao, A. R.; Habas, S.; Yang, P. *Small* **2008**, *4*, 310−325.

(19) (a) Zhang, H.; Jin, M.; Xia, Y. *Angew. Chem., Int. Ed.* **2012**, *51*, 7656−7673. (b) Lim, B.; Xia, Y. *Angew. Chem., Int. Ed.* **2011**, *50*, 76−85. (c) Quan, Z.; Wang, Y.; Fang, J. *Acc. Chem. Res.* **2013**, *46*, 191−202.

(20) (a) Jana, N. R.; Gearheart, L.; Murphy, C. J. *J. Phys. Chem. B* **2001**, *105*, 4065−4067. (b) Sun, Y.; Gates, B.; Mayers, B.; Xia, Y. *Nano Lett.* **2002**, *2*, 165−168. (c) Habas, S. E.; Lee, H.; Radmilovic, V.; Somorjai, G. A.; Yang, P. *Nat. Mater.* **2007**, *6*, 692−697. (d) Xue, C.; Millstone, J. E.; Li, S.; Mirkin, C. A. *Angew. Chem., Int. Ed.* **2007**, *46*, 8436−8439. (e) Fan, F.-R.; Liu, D.-Y.; Wu, Y.; Duan, S.; Xie, Z.-X.; Jiang, Z.-Y.; Tian, Z.-Q. *J. Am. Chem. Soc.* **2008**, *130*, 6949−6951.

(21) (a) Wade, L. G., Jr. *Organic Chemistry*, 2nd ed.; Prentice Hall: Englewood Cliffs, NJ, 1991. (b) Wang, Y.; He, J.; Liu, C.; Chong, W. H.; Chen, H. *Angew. Chem., Int. Ed.* **2015**, *54*, 2022−2051.

(22) Atkins, P.; de Paula, J. *Physical Chemistry*, 8th ed.; W.H. Freeman: New York, 2006.

(23) Markov, I. V. *Crystal Growth for Beginners: Fundamentals of Nucleation, Crystal Growth and Epitaxy*, 1st ed.; World Scientific: Singapore, 1995.

(24) Mackenzie, J. K.; Moore, A. J. W.; Nicholas, J. F. *J. Phys. Chem. Solids* **1962**, *23*, 185−196.

(25) (a) Frenken, J. W. M.; Stoltze, P. *Phys. Rev. Lett.* **1999**, *82*, 3500−3503. (b) Yu, D. K.; Bonzel, H. P.; Scheffler, M. *New J. Phys.* **2006**, *8*, 65.

(26) (a) Vitos, L.; Ruban, A. V.; Skriver, H. L.; Kollar, J. *Surf. Sci.* **1998**, *411*, 186−202. (b) Galanakis, I.; Papanikolaou, N.; Dederichs, P. H. *Surf. Sci.* **2002**, *511*, 1−12. (c) Zhang, J. M.; Ma, F.; Xu, K. W. *Appl. Surf. Sci.* **2004**, *229*, 34−42.

(27) (a) Wulff, G. Z. *Kristallogr. Mineral.* **1901**, *34*, 449−530. (b) Herring, C. *Phys. Rev.* **1951**, *82*, 87−93. (c) Henry, C. R. *Prog. Surf. Sci.* **2005**, *80*, 92−116.

(28) (a) Kumikov, V. K.; Khokonov, Kh. B. *J. Appl. Phys.* **1983**, *54*, 1346−1350. (b) Surnev, S.; Arenhold, K.; Conen, P.; Voigtländer; Bonzel, H. P. *J. Vac. Sci. Technol. A* **1998**, *16*, 1059−1065. (c) Bonzel, H. P.; Emundts, A. *Phys. Rev. Lett.* **2000**, *84*, 5804−5807.

(29) (a) Burrows, M. G. T.; Stockmayer, W. H. *Surf. Sci.* **1940**, *176*, 471−483. (b) Ertl, G.; Rau, P. *Surf. Sci.* **1969**, *15*, 443−465. (c) Shi, A.-C.; Masel, R. I. *J. Catal.* **1989**, *120*, 421−431. (d) Roberts, M. W. *Surf. Sci.* **1994**, *299*, 769−784. (e) Chen, Q.; Richardson, N. V. *Prog. Surf. Sci.* **2003**, *73*, 59−77.

(30) Wang, T.; Lee, C.; Schmidt, L. D. *Surf. Sci.* **1985**, *163*, 181−197.

(31) (a) Oura, K.; Lifshits, V. G.; Saranin, A. A.; Zotov, A. V.; Katayama, M. *Surface Science: An Introduction*, 1st ed.; Springer: Heidelberg, 2003. (b) Kolasinski, K. W. *Surface Science*, 2nd ed.; Wiley: New York, 2008.

(32) Harris, P. J. F. *Nature* **1986**, *323*, 792−794.

(33) (a) Somorjai, G. A. *J. Catal.* **1972**, *27*, 453−456. (b) Oudar, J. *Catal. Rev.—Sci. Eng.* **1980**, *22*, 171−195. (c) Bartholomew, C. H. *Adv. Catal.* **1982**, *31*, 135−242.

(34) (a) Chen, M.; Wu, B.; Yang, J.; Zheng, N. *Adv. Mater.* **2012**, *134*, 15822−15831. (b) Chiu, C.-Y.; Ruan, L.; Huang, Y. *Chem. Soc. Rev.* **2013**, *42*, 2512−2527. (c) Lohse, S. E.; Burrows, N. D.; Scarabelli, L.; Liz-Mazán, L. M.; Murphy, C. J. *Chem. Mater.* **2014**, *26*, 34−43. (d) Niu, Z.; Li, Y. *Chem. Mater.* **2014**, *26*, 72−83. (e) Ortiz, N.; Skrabalak, S. E. *Langmuir* **2014**, *30*, 6649−6659.

(35) Al-Saidi, W. A.; Feng, H.; Fichthorn, K. A. *Nano Lett.* **2012**, *12*, 997−1001.

(36) (a) Sun, Y.; Xia, Y. *Science* **2002**, *4*, 1987−1996. (b) Sun, Y.; Mayers, B.; Herricks, T.; Xia, Y. *Nano Lett.* **2003**, *3*, 955−960. (c) Wiley, B.; Sun, Y.; Mayers, B.; Xia, Y. *Chem.—Eur. J.* **2005**, *11*, 454−463. (d) Xia, X.; Zeng, J.; Oetjen, L. K.; Li, Q.; Xia, Y. *J. Am. Chem. Soc.* **2012**, *134*, 1793−1801.

(37) (a) Jin, R.; Cao, Y.; Mirkin, C. A.; Kelly, K. L.; Schatz, G. C.; Zheng, J. G. *Science* **2001**, *294*, 1901−1903. (b) Jin, R.; Cao, Y. C.;

Hao, E.; Metraux, G. S.; Schatz, G. C.; Mirkin, C. A. *Nature* **2003**, *425*, 487−490. (c) Zhang, Q.; Hu, Y.; Guo, S.; Goebl, J.; Yin, Y. *Nano Lett.* **2010**, *10*, 5037−5042. (d) Zeng, J.; Tao, J.; Li, W.; Grant, J.; Wang, P.; Zhu, Y.; Xia, Y. *Chem.—Asian J.* **2011**, *6*, 376−379. (e) Wang, Y.; Wan, D.; Xie, S.; Xia, X.; Huang, C. Z.; Xia, Y. *ACS Nano* **2013**, *7*, 4586−4594.

(38) Kilin, D. S.; Prezhdo, O. V.; Xia, Y. *Chem. Phys. Lett.* **2008**, *458*, 113−116.

(39) Zeng, J.; Zheng, Y.; Rycenga, M.; Tao, J.; Li, Z.-Y.; Zhang, Q.; Zhu, Y.; Xia, Y. *J. Am. Chem. Soc.* **2010**, *132*, 8552−8553.

(40) Peng, H.-C.; Xie, S.; Park, J.; Xia, X.; Xia, Y. *J. Am. Chem. Soc.* **2013**, *135*, 3780−3783.

(41) (a) Millstone, J. E.; Wei, W.; Jones, M. R.; Yoo, H.; Mirkin, C. A. *Nano Lett.* **2008**, *8*, 2526−2529. (b) Huang, X.; Zheng, N. *J. Am. Chem. Soc.* **2009**, *131*, 4602−4603. (c) Huang, X.; Zhang, H.; Guo, C.; Zhou, Z.; Zheng, N. *Angew. Chem., Int. Ed.* **2009**, *48*, 4808−4812. (d) Xia, X.; Choi, S.-I.; Herron, J. A.; Lu, N.; Scaranto, J.; Peng, H.-C.; Wang, J.; Mavrikakis, M.; Kim, M. J.; Xia, Y. *J. Am. Chem. Soc.* **2013**, *135*, 15706−15709.

(42) (a) Wang, C.; Daimon, H.; Lee, Y.; Kim, J.; Sun, S. *J. Am. Chem. Soc.* **2007**, *129*, 6974−6975. (b) Zhang, J.; Fang, J.; Wang, C.; Daimon, H.; Lee, Y.; Kim, J.; Sun, S. *J. Am. Chem. Soc.* **2007**, *129*, 6974−6975. (c) Kang, Y.; Ye, X.; Murray, C. B. *Angew. Chem., Int. Ed.* **2010**, *49*, 6156−6159. (d) Wu, B.; Zheng, N.; Fu, G. *Chem. Commun.* **2011**, *47*, 1039−1041.

(43) (a) Huang, X.; Tang, S.; Mu, X.; Dai, Y.; Chen, G.; Zhou, Z.; Ruan, F.; Yang, Z.; Zheng, N. *Nat. Nanotechnol.* **2011**, *6*, 28−32. (b) Dai, Y.; Mu, X.; Tan, Y.; Lin, K.; Yang, Z.; Zheng, N.; Fu, G. *J. Am. Chem. Soc.* **2012**, *134*, 7073−7080.

(44) (a) Chiu, C.-Y.; Li, Y.; Ruan, L.; Ye, X.; Murray, C. B.; Huang, Y. *Nat. Chem.* **2011**, *3*, 393−399. (b) Naik, R. R.; Stringer, S. J.; Agarwal, G.; Jones, S. E.; Stone, M. O. *Nat. Mater.* **2002**, *1*, 169−172. (c) Gugliotti, L. A.; Feldheim, D. L.; Eaton, B. E. *Science* **2004**, *304*, 850−852. (d) Heinz, H.; Farmer, B. L.; Pandey, R. B.; Slocik, J. M.; Patnaik, S. S.; Pachter, R.; Naik, R. R. *J. Am. Chem. Soc.* **2009**, *131*, 9704−9714. (e) O'Brien, M. N.; Radha, B.; Brown, K. A.; Jones, M. R.; Mirkin, C. A. *Angew. Chem., Int. Ed.* **2014**, *53*, 9532−9538.

(45) (a) Wiley, B. J.; Xiong, Y.; Li, Z.-Y.; Yin, Y.; Xia, Y. *Nano Lett.* **2006**, *6*, 765−768. (b) Zhang, Q.; Moran, C. H.; Xia, X.; Rycenga, M.; Li, N.; Xia, Y. *Langmuir* **2012**, *28*, 9047−9054.

(46) (a) Xiong, Y.; Cai, H.; Wiley, B. J.; Wang, J.; Kim, M. J.; Xia, Y. *J. Am. Chem. Soc.* **2007**, *129*, 3665−3675. (b) Sun, Y.; Zhang, L.; Zhou, H.; Zhu, Y.; Sutter, E.; Ji, Y.; Rafailovich, M. H.; Sokolov, J. C. *Chem. Mater.* **2007**, *19*, 2065−2070. (c) Yuan, Q.; Zhuang, J.; Wang, X. *Chem. Commun.* **2009**, 6613−6615.

(47) (a) Bratlie, K. M.; Lee, H.; Komvopoulos, K.; Yang, P.; Somorjai, G. A. *Nano Lett.* **2007**, *7*, 3097−3101. (b) Demortière, A.; Launois, P.; Goubet, N.; Albouy, P.-A.; Petit, C. *J. Phys. Chem. B* **2008**, *112*, 14583−14592. (c) Tsung, C.-K.; Kuhn, J. N.; Huang, W.; Aliaga, C.; Hung, L.-I.; Somorjai, G. A.; Yang, P. *J. Am. Chem. Soc.* **2009**, *131*, 5816−5822.

(48) (a) Zhang, Y.; Grass, M. E.; Kuhn, J. N.; Tao, F.; Habas, S. E.; Huang, W.; Yang, P.; Somorjai, G. A. *J. Am. Chem. Soc.* **2008**, *130*, 5868−5869. (b) Yuan, Q.; Zhou, Z.; Zhuang, J.; Wang, X. *Inorg. Chem.* **2010**, *49*, 5515−5521. (c) Zhang, Y.; Grass, M. E.; Huang, W.; Somorjai, G. A. *Langmuir* **2010**, *26*, 16463−16468.

(49) (a) Kenneth, C. *Chemical Kinetics: The Study of Reaction Rates in Solution*; Wiley-VCH: New York, 1990. (b) Wang, Y.; Peng, H.-C.; Liu, J.; Huang, C.; Xia, Y. *Nano Lett.* **2015**, *15*, 1445−1450.

(50) Zhang, H.; Li, W.; Jin, M.; Zeng, J.; Yu, T.; Yang, D.; Xia, Y. *Nano Lett.* **2011**, *11*, 898−903.

(51) Tringides, M. C., Ed. *Surface Diffusion: Atomistic and Collective Processes*; NATO ASI Series B: Physics, Vol. *360*; Plenum Press: New York and London, 1997.

(52) Shustorovich, E. *Metal-Surface Reaction Energetics: Theory and Applications to Heterogeneous Catalysis, Chemisorption, and Surface Diffusion*; Wiley-VCH: New York, 1991; p 114.

(53) Xia, X.; Xie, S.; Liu, M.; Peng, H.-C.; Lu, N.; Wang, J.; Kim, M. J.; Xia, Y. *Proc. Natl. Acad. Sci. U.S.A.* **2013**, *110*, 6669−6673.

(54) (a) Wang, X. Z.; Zhao, Z. B.; Qu, J. Y.; Wang, Z. Y.; Qiu, J. S. *Cryst. Growth Des.* **2010**, *10*, 2863−2869. (b) Liu, X. H.; Huang, R.; Zhu, J. *Chem. Mater.* **2008**, *20*, 192−197. (c) Li, J. H.; Zhou, W.; Yao, M.; Guo, L.; Li, Y. M.; Yang, S. H. *J. Am. Chem. Soc.* **2009**, *131*, 2959−2964. (d) Berkovitch, N.; Ginzburg, P.; Orenstein, M. *Nano Lett.* **2010**, *10*, 1405−1408. (e) Tian, N.; Zhou, Z. Y.; Sun, S. G. *J. Phys. Chem. C* **2008**, *112*, 19801−19801.

(55) (a) Luo, Y. R. *Comprehensive Handbook of Chemical Bond Energies*; CRC Press: Boca Raton, FL, 2007. (b) Lim, B.; Jiang, M.; Camargo, P. H. C.; Cho, E. C.; Tao, J.; Lu, X.; Zhu, Y.; Xia, Y. *Science* **2009**, *324*, 1302−1305. (c) Zhang, H.; Jin, M.; Wang, J.; Kim, M. J.; Yang, D.; Xia, Y. *J. Am. Chem. Soc.* **2011**, *133*, 10422−10425.

(56) Xie, S.; Lu, N.; Xie, Z.; Wang, J.; Kim, M. J.; Xia, Y. *Angew. Chem., Int. Ed.* **2012**, *51*, 10266−10270.

(57) Xia, X.; Zeng, J.; McDearmon, B.; Zheng, Y.; Li, Q.; Xia, Y. *Angew. Chem., Int. Ed.* **2011**, *50*, 12542−12546.

(58) Xia, X.; Zeng, J.; Zhang, Q.; Moran, C. M.; Xia, Y. *J. Phys. Chem. C* **2012**, *116*, 21647−21656.

(59) Wang, Z. L. *J. Phys. Chem. B* **2000**, *104*, 1153−1175.

(60) (a) Sun, Y.; Gates, B.; Mayers, B.; Xia, Y. *Nano Lett.* **2002**, *2*, 165−168. (b) Malikova, N.; Pastoriza-Santos, I.; Schierhorn, M.; Kotov, N. A.; Liz-Márzan, L. M. *Langmuir* **2002**, *18*, 3694−3697. (c) Jana, N. R.; Gearheart, L.; Murphy, C. J. *Adv. Mater.* **2001**, *13*, 1389−1393. (d) Huang, X.; Zheng, N. *J. Am. Chem. Soc.* **2009**, *131*, 4602−4603. (e) Yang, H.; He, S.; Tuan, H. *Langmuir* **2014**, *30*, 602−610. (f) Pietrobon, B.; McEachran, M.; Kitaev, V. *ACS Nano* **2009**, *3*, 21−26. (g) Zhang, Q.; Hu, Y.; Guo, S.; Goebl, J.; Yin, Y. *Nano Lett.* **2010**, *10*, 5037−5042. (h) Millstone, J. E.; Hurst, S. J.; Métraux, G. S.; Cutler, J. I.; Mirkin, C. A. *Small* **2009**, *5*, 646−664.

(61) (a) Murphy, C. J.; Jana, N. R. *Adv. Mater.* **2002**, *14*, 80−82. (b) Nikoobakht, B.; El-Sayed, M. A. *Chem. Mater.* **2003**, *15*, 1957−1962. (c) Walsh, M. J.; Barrow, S. J.; Tong, W.; Funston, A. M.; Etheridge, J. *ACS Nano* **2015**, *9*, 715−724.

(62) Wiley, B. J.; Chen, Y.; McLellan, J. M.; Xiong, Y.; Li, Z.-Y.; Ginger, D.; Xia, Y. *Nano Lett.* **2007**, *7*, 1032−1036.

(63) Cobley, C. M.; Rycenga, M.; Zhou, F.; Li, Z.; Xia, Y. *Angew. Chem., Int. Ed.* **2009**, *48*, 4824−4827.

(64) Zeng, J.; Zhu, C.; Tao, J.; Jin, M.; Zhang, H.; Li, Z.-Y.; Zhu, Y.; Xia, Y. *Angew. Chem., Int. Ed.* **2012**, *51*, 2354−2358.

(65) Zhu, C.; Zeng, J.; Tao, J.; Johnson, M. C.; Schmidt-Krey, I.; Blubaugh, L.; Zhu, Y.; Gu, Z.; Xia, Y. *J. Am. Chem. Soc.* **2012**, *134*, 15822−15831.

(66) Liu, S.; Yue, J.; Gedanken, A. *Adv. Mater.* **2001**, *13*, 656−658.

(67) Jin, M.; Zhang, H.; Wang, J.; Zhong, X.; Lu, N.; Li, Z.-Y.; Xie, Z.; Kim, M. J.; Xia, Y. *ACS Nano* **2012**, *6*, 2566−2573.

(68) Xia, X.; Xia, Y. *Nano Lett.* **2012**, *12*, 6038−6042.

(69) Wang, Y.; Xie, S.; Liu, J.; Park, J.; Huang, C. Z.; Xia, Y. *Nano Lett.* **2013**, *13*, 2276−2281.

(70) Peng, H.-C.; Park, J.; Zhang, L.; Xia, Y. *J. Am. Chem. Soc.* **2015**, *137*, 6643−6652.

(71) (a) Zheng, H.; Smith, R. K.; Jun, Y.-W.; Kisielowski, C.; Dahmen, U.; Alivisatos, A. P. *Science* **2009**, *324*, 1309−1312. (b) Sun, Y.; Wang, Y. *Nano Lett.* **2011**, *11*, 4386−4392. (c) Sutter, E.; Jungjohann, K.; Bliznakov, S.; Courty, A.; Maisonhaute, E.; Tenney, S.; Sutter, P. *Nat. Commun.* **2014**, *5*, 4946.

(72) (a) Wiley, B.; Herricks, T.; Sun, Y.; Xia, Y. *Nano Lett.* **2004**, *4*, 1733−1739. (b) Xiong, Y.; Chen, J.; Wiley, B.; Xia, Y.; Aloni, S.; Yin, Y. *J. Am. Chem. Soc.* **2005**, *127*, 7332−7333. (c) Im, S.; Lee, Y.; Wiley, B.; Xia, Y. *Angew. Chem., Int. Ed.* **2005**, *44*, 2154−2157. (d) Zheng, Y.; Zeng, J.; Ruditskiy, A.; Liu, M.; Xia, Y. *Chem. Mater.* **2014**, *26*, 22−33.

(73) Chen, J.; Herricks, T.; Xia, Y. *Angew. Chem., Int. Ed.* **2005**, *44*, 2589−2592.

(74) (a) Tao, A.; Sinsermsuksakul, P.; Yang, P. *Angew. Chem., Int. Ed.* **2006**, *45*, 4597−4601. (b) Korte, K. E.; Skrabalak, S. E.; Xia, Y. *J. Mater. Chem.* **2008**, *18*, 437−441.